運輸省港湾技術研究所

港湾技術研究所報告

REPORT OF THE PORT AND HARBOUR RESEARCH INSTITUTE

MINISTRY OF TRANSPORT

VOL. 24 NO. 1 MAR. 1985

NAGASE, YOKOSUKA, JAPAN

港湾技術研究所報告 (REPORT OF P.H.R.I.)
第24巻 第1号 (Vol. 24, No. 1), 1985年3月 (Mar. 1985)

目 次 (CONTENTS)

REPORT OF THE PORT AND
HARBOUR RESEARCH INSTITUTE
Vol. 24, No. 1 (Mar. 1985)

3. Nonlinear Properties of Arc-Shaped Concrete Members

Osamu KIYOMIYA*
Hiroshi YOKOTA**

Synopsis

Arc-shaped configurations are recently introduced to wave dissipating members, revetments and other offshore structures. The arc-shaped members in offshore structures are subjected to large alternate wave forces, that is, from the outside to the inside of the member and from the inside to the outside. Therefore, being different from for land structures as to the direction of forces, the mechanical properties of the member subjected to alternate forces must be considered in design works and in structural analyses. The main materials for these arc-shaped members are reinforced concrete and prestressed concrete. However, mechanical properties of the member subjected to alternate forces are not clarified sufficiently in the elastic and plastic range of the materials.

Loading tests and nonlinear finite element analysis were carried out to know the nonlinear properties of arc-shaped members subjected to alternate forces. In particular, not only the force of resistance but also nonlinear properties were investigated, which were referred to the ability of deflection, energy absorption, mechanisms of fracture and so on. Moreover, crack formation was examined from the viewpoint of durability. The present paper describes these nonlinear properties through the experimental and analytical results.

The following main results were obtained.

1) Mechanical properties of the arc-shaped members such as the force of resistance, ductility, the ability of energy absorption, formation of cracks, mechanisms of fracture, etc. depend on the directions of loadings.
2) The force of resistance of the arc-shaped members can be estimated well by the ordinary limit state design method for straight members considering of the moment distribution at plastic hinges.
3) The formulae for the crack width in concrete proposed by the limit state design method (JSCE) and CEB-FIP (in 1978) gave the maximum crack width of the arc-shaped member on the safe side.
4) The finite element method in consideration of the material nonlinearity and the formation of plastic hinges can explain the experimental results of the arc-shaped members.

* Chief of Subaqueous Tunnels and Pipelines Laboratory, Structures Division
** Member of Subaqueous Tunnels and Pipelines Laboratory, Structures Division

港湾技術研究所報告
第24巻 第1号 (1985. 3)

3. 曲面部材の非線形挙動の解析

清 宮 理*・横 田 弘**

要 旨

コンクリート製曲面構造は，橋梁でのアーチ，トンネルの支保工，原子炉容器等に用いられている。海洋構造物でも近年，消波構造，円形護岸等に曲面構造がいくつか導入されてきている。これらの海洋構造物での曲面構造は，従来の陸上での構造と異なった自然環境，特に厳しい波浪環境に置かれる。

この場合，曲面部材には，部材の外側及び内側の両方向から繰り返し外力が作用する。このような外力の作用下での部材の力学的性質に関しては，十分明らかになっていない。特に，構造物の安全性を検討するためには，耐力のみならず変形能力，エネルギー吸収能力，破壊のメカニズム等の非線形挙動を明らかにしておく必要がある。また，耐久性の観点から，過度のコンクリートひびわれの発生を制限しなければならない。

このようなことから，模型載荷実験及び有限要素法による解析を通して，交番加力を受ける曲面部材の非線形挙動の解析を行った。

本研究で得られた主要な結論は，以下のとおりである。

1) 曲面部材は加力の方向によって，終局耐力，じん性，エネルギー吸収能力，ひびわれの発生，破壊の形態などの力学的性状が大きく異なった。
2) 塑性ひんじの発生に伴うモーメントの再配分を考慮した上で，直線部材を対象とした従来の終局強度理論を用いると，曲面部材の終局耐力を精度良く推定できた。
3) 曲面部材に発生するひびわれ幅は，限界状態設計法（土木学会）及び CEB-FIP (1978年) で提案されている算定式で実用上安全側に計算された。

* 構造部 沈埋構造研究室長
** 構造部 沈埋構造研究室

CONTENTS

1. Introduction

1.1 General

Japan, which is located at the north west of the Pacific Ocean, is surrounded by the sea. The eastern coastline of Japan faces the Pacific Ocean and the western coastline faces the Japan Sea. The space of the sea around Japan should be utilized actively because of her small area of the land, dense population and high industrialization. Exploitation of the sea has being steadily progressed in Japan. Not only the extraction of natural resources from the sea but the construction of various types of offshore structures is intensively demanded. Man-made islands where industrial facilities, power plant etc. are built, and breakwaters which secure calm water area can be cited by way of examples as the offshore structures. The main materials of the offshore structures are steel and concrete. Reinforced concrete or prestressed concrete is used generally for the offshore structures in view of durability of the structures and economy of construction cost. The offshore structures are subjected to strong wave forces due to storms including typhoons, and therefore the safety of the offshore structures for strong wave forces should be secured. Several new structural devices are proposed to dissipate the wave energy or to decrease the ground reacting force. One of them is an arc-shaped wave dissipating member. This member is attached in front of the offshore structures, and a wave dissipating chamber is formed with these members and a rear vertical wall as shown in Fig. 1. Hydraulic tests have been carried out to know the wave forces acting on the members and to confirm the dissipating efficiency of wave energy. A prototype breakwater caisson with these arc-shaped members has been set at Funakawa Port in Akita Prefecture at about 450 km north of Tokyo, for the purpose of field experiments, to confirm the efficiency and the performance in the site and to know the behavior of the breakwater for waves[1]. Effectiveness of the arc-shaped wave dissipating members has been confirmed by the hydraulic test and the field observation. Therefore, several breakwaters with these arc-shaped members are being planed at several ports and one is already under construction. Thus the arc-shaped wave dissipating

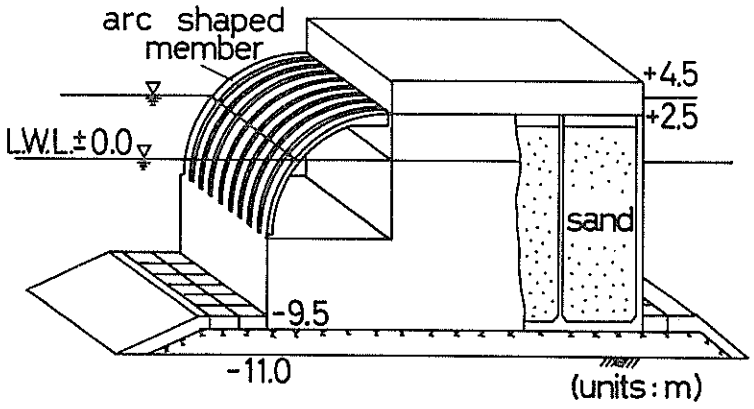

Fig. 1 A Breakwater with Arc-Shaped Wave Dissipating Members (set at Funakawa Port)

members will make practical use of the offshore structures. It is necessary to obtain the fundamental characteristics of the toughness and deformation of the members for wave force beside hydraulic characteristics. The wave forces are applied on both sides of the members, namely from the outside as well as from the inside. Strong wave forces due to wave breaking in the chamber occur. The safety of the members against wave forces should be appropriately estimated at both wave breaking and repeated waves which sometimes give fatigue damage for the members. This report describes the fundamental characteristics of the strength and deformation of the arc-shaped wave dissipating members, which have been investigated by means of loading tests and numerical simulations. The ultimate strength and fracture process, namely nonlinear properties of the members are main research items in this report. Fatigue strength of them is not mentioned in this report.

1.2 Review of Previous Researches

Cylindrical vessels (silos, fluid containers, etc.), concrete pipes, arches in bridges, supports of tunnels and barrel vaults in buildings are the structures with arc-shaped configurations. The arc-shaped members in these structures resist both the bending moment and the axial force. Circumferential stresses and radial stresses occur in the section of the member when loads are applied upon them. The direction of stresses in the arc-shaped members differ from that in the straight members because of their curvature. After the moments and axial forces are calculated by structural analyses such as the shell theory and the finite element method, the width and thickness, arrangement of reinforcing bars, etc. in the sections of the arc-shaped members are determined as though they were straight members in most of design practice. This design procedure was endorsed by R. H. Dawoud[2]. He examined the difference of stresses between the arc-shaped members and the straight members subjected to the bending moment, using the elastic theory. According to his research work, when a curvature index (the ratio of the thickness to the radius of curvature of the member) does not exceed 0.2, the design of the arc-shaped members' sections can be treated as that of the straight members' sections. When the curvature index is greater than 0.2, the effect of the radial stresses is not negligible in the design. Namely, the compressive stresses in concrete appear below the neutral axis. When the direction of the bending moment is reversed, the stresses in concrete below the neutral axis become less. Kawakami et al.[3] proposed the plastic design method of the reinforced concrete arc-shaped members by considering the nonlinearity of the materials. The strain distribution of the section is assumed to be a parabolic function. The validity of proposed method was examined by comparison with the experimental results of reinforced concrete pipes. Heger et al.[4] carried out the loading tests of arc-shaped reinforced concrete pipes to know their ultimate strength. Through the test results, they proposed the design equation of the radial reinforcement for radial stresses.

The structural analysis of shells was initiated by A. E. H. Love[5], who developed the theory of shells at the beginning of 1920's. H. Reissner developed the bending theory of cylindrical shell and Z. Bazant advanced to the bending theory of thick shells. The theory of shells has been established by these theoretical researches. S. Timoshenko and S. Woinowsky-Krieger[6] wrote out the theory of shell in their book. The theory of shells has been applied for concrete shell roofs by H. Lundgren et al.[7] H. Lundgren analyzed shells by the elastic theory and the fracture theory. The ultimate strength of the concrete shell was estimated by them.

1.3 Objectives and Scope

The main objective in this research work is to know the static characteristics of the arc-shaped reinforced/prestressed concrete members. Items of the research work are as follows:

① loading test of arc-shaped members
② comparison between the calculated results by the limit state design method and the experimental results
③ comparison between the calculated results by the finite element method and the experimental results
④ proposal of the finite element model considering the nonlinearity of materials and plastic hinges

(1) Loading Test

The present objective of loading test of the arc-shaped members is to know the mechanical properties of these members. The results are arranged as in the following:

① load-deflection relationship
② deflection of members and strain in reinforcing bars and concrete
③ mechanisms of plastic hinges formations: location of plastic hinges and moment redistribution to other parts of members
④ crack formation and crack widths
⑤ ductility factor and energy dissipated

Though wave forces are distributed on arc-shaped members in the site, the loading is treated as the concentrated load, and is applied on the midspan of the test specimen in the experiment. The directions of loading are both from the inside and from the outside, by considering the alternation of the direction of existing wave forces. Thus, differences of the static characteristics of beams according to the load directions are scrutinized in this study.

(2) Limit State Sesign

The arc-shaped members in the experimental breakwater caisson constructed tentatively at Funakawa Port was designed by the limit state design method[8]. The allowable stress design method is still available in Japan. The limit state design method has been gradually introduced into the design work for the offshore structures made of prestressed/reinforced concrete. Although many limit states are listed[9], the ultimate limit state and the serviceability limit state are considered in this study. The ultimate strength is compared between the values from experiments and those from design procedures. The crack formation is related to the serviceability limit state. If sea water soaks into the cracks ceaselessly, the reinforcing steel suffers corrosion and the durability of materials is degraded. The maximum crack width is restricted in the limit state design in view of the durability[10].

(3) Finite Element Method

The finite element method is one of the best means to simulate the precise characteristics of the arc-shaped members and overall structures. This method plays an important role in the analysis or estimation of the safety of structures with complex configurations. In this study, nonlinear properties of stress-strain relationships of materials and the yield hinge mechanism are taken into consideration in the calculation model. The calculated results are compared with the experimental results. The validity of the finite element model in this report is evaluated through the comparison.

The finite element method has been progressing and applying to the shells in association with the increase in the capacity of computers and the reduction of com-

putation time. This method can be applied for various kinds of shell-type structures. A plane shell element which combined the bending and membrane elements was used at the first stage of analysis of shells. Several elements with high degree of accuracy have been proposed. These elements raise reliability of structural analysis by the finite element method.

2. Design of Arc-Shaped RC and PC Members

2.1 Acting Force and Design Condition

(1) Acting Force

Arc-shaped members described in this report are attached in front of breakwater caissons to dissipate the wave energy. Each arc-shaped member is a quarter circle in the side view as shown in Fig. 1. A wave dissipating chamber in the breakwaters is surrounded by the arc-shaped members, a perpendicular wall and a horizontal wall. A part of waves are reflected directly by the arc-shaped members, the other part of waves enter the chamber to dissipate the wave energy due to wave breaking. The typical state of the waves with large wave height, reached the dissipating chamber, is shown in Fig. 2. The states of the waves depend on the wave condition and tidal condition. Generally speaking, when the water surface ascends, wave forces act on the arc-shaped members from the outside towards the inside. After the water surface reaches the top of the breakwater, i.e., capping part, the direction of wave forces changes from inward to outward. The impact wave forces occur in the dissipating chamber. The maximum wave force occurs at this moment. The wave forces from the inside gradually decrease during descending of the water surface. Figure 3 shows the wave forces (P_w) along the axis of the arc-shaped member which can be approximately calculated as Eq. (2.1) from the results of hydraulic model tests[11].

$$P_w = P_A \cos^2\theta + P_B \sin^2\theta \tag{2.1}$$

The two conditions are used at the design work of the arc-shaped members.

$$\left.\begin{array}{lll} ① & P_A = 1.0 w_0 H, & P_B = 0 \quad \text{(from the outside)} \\ ② & P_A = 0, & P_B = -1.5 w_0 H \quad \text{(from the inside)} \end{array}\right\} \tag{2.2}$$

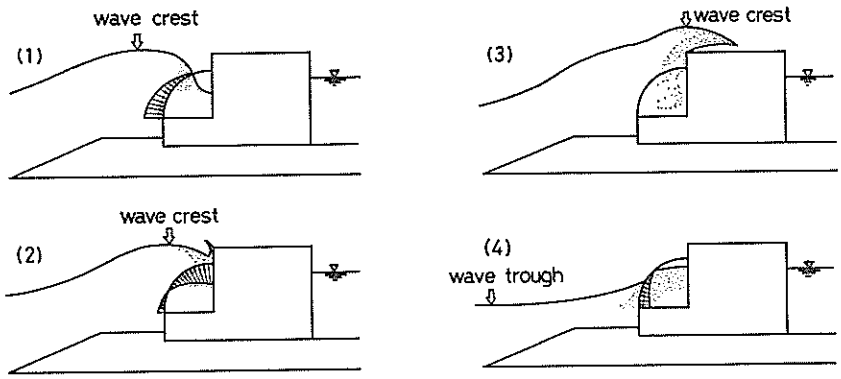

Fig. 2 Wave Forces Acting on the Arc-Shaped Member[11]

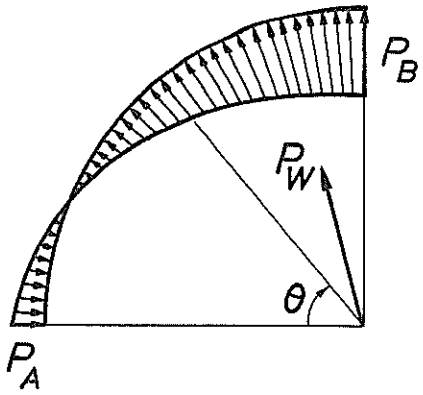

Fig. 3 Distribution of Wave Force.

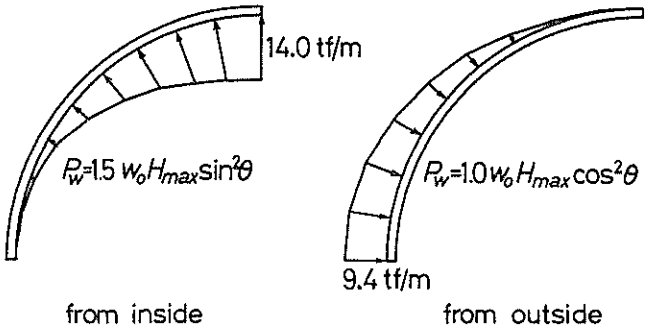

Fig. 4 Design Wave Forces for the Prototype Arc-Shaped Member

where w_0 denotes the unit weight of sea water and H is the wave height. Both conditions are applied at the times of the ascending of the water surface.

Figure 4 shows the distributions of design wave forces acting on the arc-shaped wave dissipating member under the above two conditions.

(2) Design Condition

Wave forces act on the arc-shaped members from the outside and from the inside alternately. When the wave forces act from the inside, tensile stresses occur in the arc-shaped member. It is possible that this tensile stress gives cracks to the arc-shaped member made of reinforced concrete. A great crack width should be restricted because of corrosion damage to reinforcing bars and degradation of concrete material. For the arc-shaped member, the prestressed concrete is used in order not to generate cracks in concrete. Namely, the prestress force is determined so as to resist the tensile stress and not to generate cracks in the arc-shaped member. Although prestressed concrete is used for the arc-shaped members in the breakwaters, the caisson besides the dissipating members are made of reinforced concrete. The reinforced concrete caisson and the arc-shaped members are built in the caisson yard. The arc-shaped members are attached and joined by cast-in-place concrete and PC bars to the RC caisson. An area of the members' section, prestress force, reinforcement, etc. are determined to

prevent the generation of cracks in the members at the time of the application of design wave forces. The design method used is "Design Criteria for Prestressed Concrete Port and Harbour Structures (provisional)"[12].

The summary of the design condition of the experimental breakwater at Funakawa Port is shown below.

① tide level H.W.L. $=+0.5$ m
L.W.L. $=\pm 0.0$ m
M.S.L. $=+0.2$ m

② mud line -11.0 m

③ design wave $H_{max}=9.47$ m
$H_{1/3}=7.14$ m
$T_{1/3}=14.0$ s
angle of incidence $=0°$
return period $=50\sim100$ years

④ strength of materials
design strength of concrete $=450$ kgf/cm^2 ($\gamma_c=1.5$)
prestressing wires $12\phi7$ (JIS G 3536 SWPR1)
ultimate tensile stress 110 kgf/mm^2 ($\gamma_m=1.15$)
yield stress 95 kgf/mm^2
prestressing stress 10 kgf/cm^2

2.2 Limit State Design Method

(1) Ultimate Strength

The ultimate strength is scrutinized for both the bending moment and the shear force. The estimation of the ultimate strength of the members subjected to the bending moment and axial force is based on the following hypotheses:

① The strains in a section above and below the neutral axis are in proportion to the distance from the axis as shown in Fig. 5.

② Concrete is not capable of resisting tensile stresses.

③ The stress (σ_c')-strain (ε_c') relationships and strength properties of concrete are presented in Eq. (2.3) and shown in Fig. 6.

$$\left.\begin{aligned}\sigma_c'&=k_1 f_{cd}'\times\frac{\varepsilon_c'}{0.002}\left(2-\frac{\varepsilon_c'}{0.002}\right) \quad (0\leqq\varepsilon_c'\leqq0.002)\\ \sigma_c'&=k_1 f_{cd}' \quad (0.002<\varepsilon_c'\leqq0.0035)\end{aligned}\right\} \tag{2.3}$$

where f_{cd}' denotes the design compressive strength of concrete.

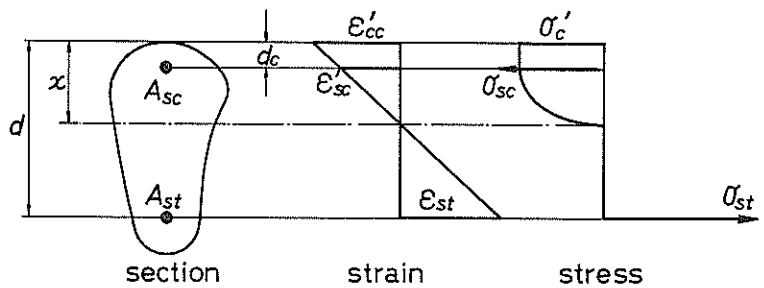

Fig. 5 Idealized Strain and Stress Distributions in a Section

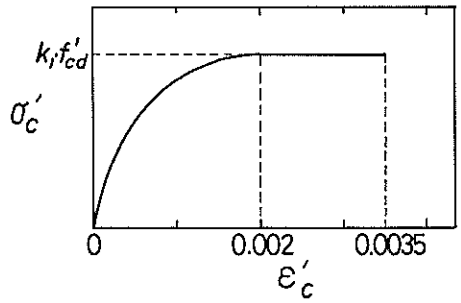

Fig. 6 Idealized Stress-Strain Curve of Concrete

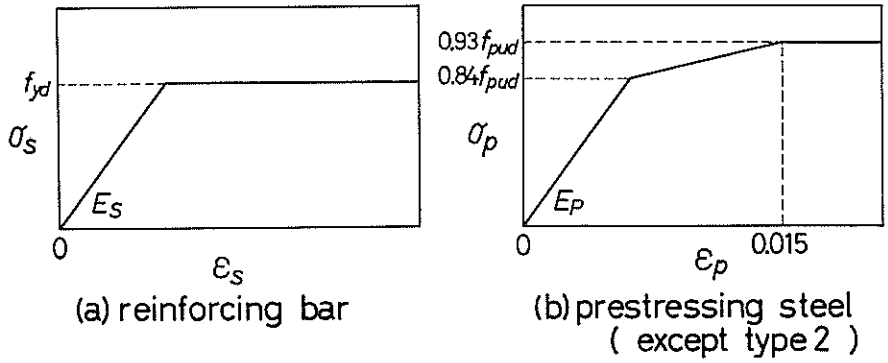

Fig. 7 Idealized Stress-Strain Curves of Steel

④ The stress (σ_s or σ_p)-strain (ε_s or ε_p) relationships of steels are presented in Fig. 7.

(a) for reinforcing bar

$$\left.\begin{aligned} &\sigma_s = E_s \varepsilon_s \quad \left(0 \leqq \varepsilon_s < \frac{\varepsilon_{sy}}{E_s}\right) \\ &\sigma_s = f_{yd} \quad \left(\frac{\varepsilon_{sy}}{E_s} \leqq \varepsilon_s\right) \end{aligned}\right\} \tag{2.4a}$$

where f_{yd} denotes the design yield strength and E_s is the modulus of elasticity.

(b) for prestressing bar (except type 2)

$$\left.\begin{aligned} &\sigma_p = E_p \varepsilon_p \quad \left(0 \leqq \varepsilon_p < \frac{0.84 f_{pud}}{E_p}\right) \\ &\sigma_p = \frac{0.09 f_{pud}}{0.015 - 0.84 f_{pud}/E_p} + 0.84 f_{pud} \quad \left(\frac{0.84 f_{pud}}{E_p} \leqq \varepsilon_p < 0.015\right) \\ &\sigma_p = 0.93 f_{pud} \quad (0.015 \leqq \varepsilon_p) \end{aligned}\right\} \tag{2.4b}$$

where f_{pud} denotes the design tensile strength and E_p is the modulus of elasticity.

The ultimate strength of the members subjected to the bending moment and the axial force can be calculated by Eq. (2.5). For a given distance x to the neutral axis, the axial force of resistance (N_u') and the bending moment of resistance (M_u) can be calculated.

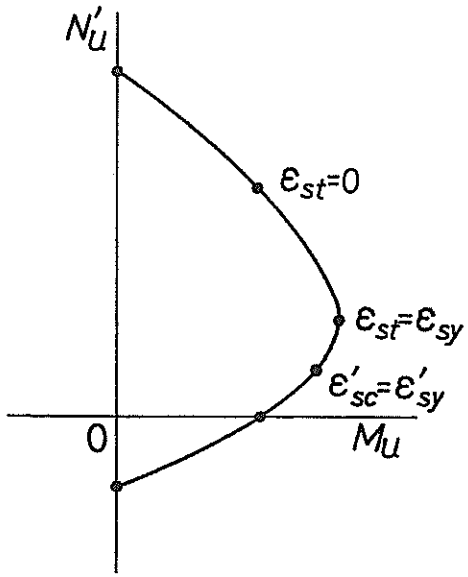

Fig. 8 Interaction Diagram

$$\left.\begin{aligned} N_u' &= C' + T_{sc}' - T_{st} \\ M_u &= C'(h/2-\beta x) + T_{sc}'(h/2-d_c) + T_{st}(d-h/2) \end{aligned}\right\} \tag{2.5}$$

where C', T_{sc}' and T_{st} denote the resultant forces in concrete, compressive reinforcement and tensile reinforcement, respectively. Furthermore, h denotes the overall thickness, and d_c and d are the distances from the extreme compressive fiber to the centroids of reinforcements.

The ultimate flexural moment is associated with the ultimate compressive strength. This interaction diagram of bending moment and axial force is shown in Fig. 8.

The shear strength is discussed in **5.2.**

(2) Crack Width

Several equations regarding the crack width have been proposed. The equation in the limit state design is determined with reference to equations proposed by Gergely-Lutz, Kakuta, Beeby, Nawy-Huang and others[13] as below.

$$w=\gamma_a \frac{k_3 \Delta\sigma_s}{K} \sqrt[3]{c_\phi \left(c+\frac{\phi}{2}\right)^2} \tag{2.6}$$

where w: crack width, $\Delta\sigma_s$: stress increment in reinforcement in the cracked section, c_ϕ: spacing of bars, c: concrete cover thickness, ϕ: diameter of steel, K: constants, and γ_a and k_3: coefficients.

The cover thickness of concrete to the reinforcement is specified as 7 cm for the sprash zone, and 5 cm for the atmospheric and submerged zones in "Technical Standard for Port and Harbour Facilities in Japan (1980)"[10]. Criteria of the allowable crack widths are listed in Table 1. The above values of cover thickness are to restrict the crack width below 0.2 mm in the sprash zone. The stress of reinforcements is related to the crack width as presented Eq. (2.6). Namely, incremental values of bar stresses due to permanent loads are restricted as listed in Table 2. There are many reasons that cracks

Table 1 Allowable Crack Width

(units : cm)

	types of steel	zones of exposure	
		submerged and atmospheric zones	sprash zone
reinforced concrete	deformed bar	0.004 c	0.0035 c
	round bar	0.004 c	0.0035 c
prestressed concrete	deformed bar	0.004 c	0.0035 c
	prestressing bar	0.0035 c	0.003 c

Table 2 Restricted Incremental Bar Stress Due to Permanent Load

(units : kgf/cm²)

	types of steel	zones of exposure	
		submerged and atmospheric zones	sprash zone
reinforced concrete	deformed bar	1000	800
	round bar	800	600
prestressed concrete	deformed bar	1000	800
	prestressing bar	800	600

occur in the structures. Cracks due to the performance and material properties cannot be estimated in design work. In the serviceability limit state design, the cracks due to the bending moment and the shear forces are taken into account. Cracks cause damage to the structures. For example, corrosion of the reinforcing bars, degradation of water-tightness, and degradation of concrete surfaces are associated with the formation of cracks. The limit state of cracks depends on the zones of exposure of the structures. Three zones of exposure should be considered, that is, the atmospheric zone, the splash zone and the submerged zone. Cracks due to the shear force have greater effects on the structures than those due to the bending force, concerning with durability and permeability. Although researches of cracks due to the shear force have not been progressed sufficiently, it is reported that cracks due to shear forces exercise little effects on structures when the strains of stirrup are within the level of 1000×10^{-6} and the service load in use is less than 0.5~0.7 times the ultimate load. The crack due to the shear force, however, will be an important problem which should be clarified in future.

3. Description of Experimental Work

3.1 General

An experimental work has been conducted so as to know the mechanical properties of arc-shaped members subjected to alternate forces. Namely,

① strengths of members at cracking, yielding and ultimate
② deflection, ductility factor and ability of energy absorption
③ strains in concrete and reinforcement
④ formation of cracks
⑤ fracture mechanism, and so on.

The test specimens employed for the experimental work are made of reinforced concrete (RC) and prestressed concrete (PC). A total of ten specimens are manufactured and tested. The overall sizes are the same among the specimens. Therefore, various

fundamental parameters such as the specimen sizes, areas of reinforcements, strengths of materials and prestressing force are not examined in this experimental program.

The test specimen in this study is modeled on prototype wave dissipating members which are subjected to wave force repeatedly on site. The loading is, however, applied under static conditions, and dynamic effects (period, amplitude and so on) are not considered.

3.2 Test Specimen

The test specimen employed for the experiment is designed on the basis of the arc-shaped wave dissipating member in the experimental breakwater having been built at Funakawa Port (see Chap. **2**). The test specimen is designed to a scale of approximately 0.2 to 0.3 of the prototype member, but is not an exact scale model. Details of the test specimen are shown in Fig. 9. The test specimen is a quarter circle in the side view, and has two blocks at both ends. The test specimen is set to the testing floor and wall through these blocks with 24 prestressing bars. Moreover, the fixed end condition can be satisfied. The section of the member is rectangular. The overall dimensions of the specimens are common: the centroid radius is 160 cm, and the width and the thickness (height) of the section are 27 cm and 11 cm, respectively. The block has the dimensions of 74 cm in length, 40 cm in width and 30 cm in height.

The test specimen is reinforced by ten longitudinal deformed bars of 6 mm in diameter (conformed to JIS G 3112 SD30-D6). The depth to the centroid of outer rein-

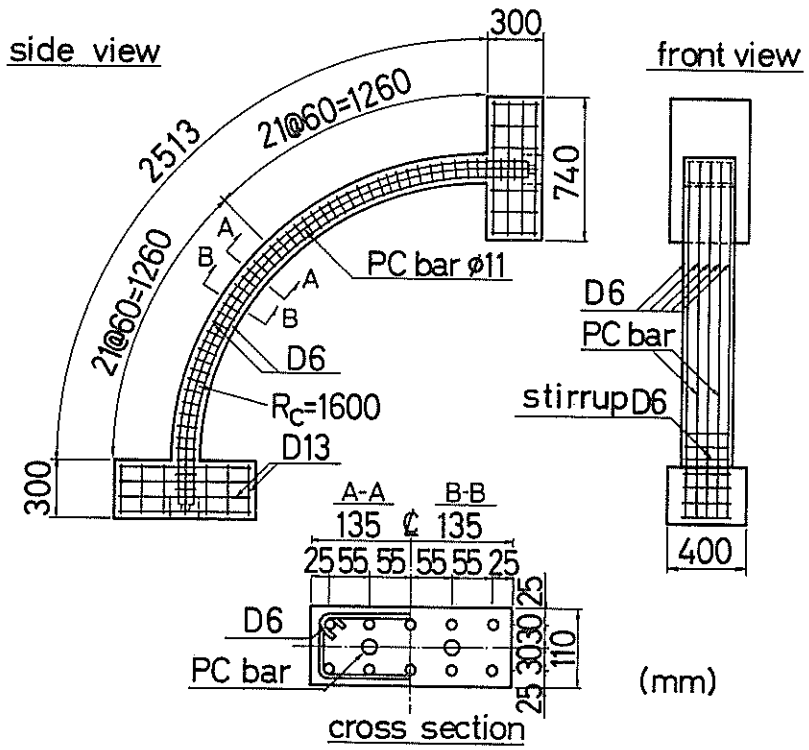

Fig. 9 Details of the Test Specimen

forcing bars is 2.5 cm, and that of inner reinforcing bars is 8.5 cm. Deformed 6 mm diameter bars are also employed for stirrups in the specimen and the spacing of them are about 6 cm. Two prestressing bars are arranged additionally at the centroid of the section for the PC specimens. The prestressing bar has a diameter of 11 mm. Effective prestress in PC specimen is about 20 kgf/cm² at the midspan section, which is introduced by the bonded post-tensioning system.

3.3 Material Properties

Concrete for the test specimens is made by the following materials.

① Cement : High early strength portland cement conformed to JIS R 5210. Table 3 lists the physical and chemical properties of the cement.

② Aggregate : Crushed sand and crushed stone produced at Hachioji located west of Tokyo. 10 mm maximum size aggregate is used because of the congested reinforcements. Teble 4 lists the properties of the aggregate. The grading distribution of the aggregate is shown in Fig. 10.

③ Water reducing agent: Lignin sulphonate type is used. Air entraining agent is added.

Table 3 Properties of the Cement

specific gravity	fineness		setting			soundness
	Blaine (cm²/gf)	88μm residual (%)	water (%)	initial (h-min)	final (h-min)	
3.12	4140	0.2	29.9	2-20	3-24	good

flow	flexural strength (kgf/cm²)				compressive strength (kgf/cm²)			
	1 day	3 days	7 days	28 days	1 day	3 days	7 days	28 days
245	35	55	68	80	130	252	356	469

chemical composition (%)								
ig. loss	insol.	SiO_2	Al_2O_3	Fe_2O_3	CaO	MgO	SO_3	total
1.1	0.1	20.7	4.9	2.9	65.8	1.4	2.8	99.7

Table 4 Properties of the Aggregate

	specific gravity	bulk density (kgf/m³)	finess modulus	absorption (%)	88μm sieve test (%)	soundness (%)
coarse	2.63	—	6.19	0.68	—	—
fine	2.60	1666	2.97	1.69	2.3	0.4

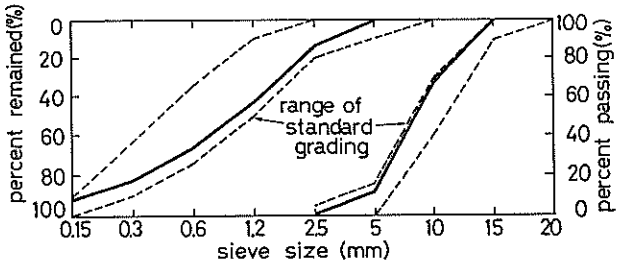

Fig. 10 Grading Curve of the Aggregates

Table 5 Properties of the Steel

type	diameter (mm)	yield stress (kgf/mm²)	ultimate stress (kgf/mm²)	elongation (%)	modulus of elasticity (kgf/mm²)
deformed bar	6	37.2	52.8	27.5	2.10×10^4
deformed bar	13	38.0	55.0	25	2.10×10^4
PC bar	11	143.0	152.0	9	2.06×10^4

Table 6 Cement Paste for Grouting

	mix proportion for one batch					flow
	cement (kgf)	water (kgf)	water-cement ratio	water reducing agent (gf)	aluminum powder (gf)	(s)
PC-1	20	8	0.40	50	1.4	10.5
others	40	17	0.425	100	2.8	10.5

	test for bleeding and expansion					compressive strength	
	sample	after 3 hours		after 24 hours		7 days	28 days
	(ml)	bleeding	expansion	bleeding	expansion	(kgf/cm²)	
PC-1	380	1.3%	2.6%	0.0%	2.6%	216	233
others	413	2.4%	4.8%	0.0%	5.6%	220	233

Steel reinforcing bars are conformed to JIS G 3112 SD30, and the diamter is 6 mm for the beam part and 13 mm for the blocks. Prestressing bar with the diameter of 11 mm conformed to JIS G 3109 C-1 (SBPR 110/125). Mechanical properties of the reinforcing bars and prestressing bars are presented in Table 5. After the introduction of prestressing, cement paste is grouted into sheaths in the PC specimens. The properties of the grouting cement paste are presented in Table 6.

3.4 Fabrication

The mix proportion of the concrete is listed in Table 7. The specific mixture is designed by the following items.

① Average compressive strength at 28 days is 400 kgf/cm².
② Initial slump is 8±2.5 cm.
③ Air content is 5±1%.

Concrete is mixed in a batching plant, and then placed into a mould. Slump, air content and initial temperature of the concrete are measured before the placing of concrete, so as to confirm the design condition. Of the ten specimens fabricated, five are reinforced concrete and other five are prestressed concrete. Table 8 lists the pro-

Table 7 Specified Mix for the Concrete

specified concrete strength (kgf/cm²)	slump (cm)	maximum size of aggregate (mm)	air content (%)	water-cement ratio (%)	fine agg. ratio (%)	weight of materials (kgf/m³)				water reducing agent (l/m³)
						water	cement	fine agg.	coarse agg.	
400	8±2.5	10	5±1	57.7	49.5	169.3	293	884	913	2.93

Table 8 Properties of the Concrete

No.	slump (cm)	air content (%)	concrete temperature (°C)	compressive strength at 28 days (kgf/cm²)
PC-1	6.8	4.7	10	437
PC-2	10.0	5.6	10	366
PC-3	8.6	4.8	15	379
PC-4	10.0	4.8	12	417
PC-5	6.3	5.9	15	418
RC-1	10.3	5.2	13	415
RC-2	7.9	4.2	11	450
RC-3	7.9	6.0	13	414
RC-4	10.0	5.6	11	377
RC-5	9.2	5.4	11	439

Table 9 Strain in PC Bars at Prestressing

No.	age (days)	strain in PC bars ($\times 10^{-6}$)	
		1	2
PC-1	9	1938	1718
PC-2	8	1810	1746
PC-3	4	1820	1833
PC-4	8	1999	1705
PC-5	3	1974	1742

*) objective strain is 1855×10^{-6}

perties of the concrete at the time of placing and the compressive strength at 28 days. Concrete is compacted by rod type vibrators.

The casting moulds are removed at 1 or 2 days and cured by means of cover sheets till the time of the loading test for the RC specimens. For the PC specimens, they are cured by wet mats till prestressing (moist curing), and thereafter by sheet curing till the loading test.

Prestress is introduced in the PC specimen in accordance with JSCE Standard for Prestressed Concrete[4]. In order to obtain the value of effective prestress (20 kgf/cm²) at the time of loading test, prestressing force is determined by considering the various factors for loss of prestress. Calculation of prestressing force and loss of prestress are given in **Appendix A.** Table 9 lists strains in the prestressing bars at the time of prestressing. Distributions of the strain in prestressing bars at prestressing are described in **Appendix B.** After the introduction of prestress, cement paste grouting is performed.

3.5 Test Procedures and Instrumentation

Loading tests are conducted at the testing floor and wall at the Port and Harbour Research Institute. Figures 11 and 12 show the test setup. The test specimen is fixed to the floor and wall at both blocks by 24 prestressing bars (diameter of 17 mm). The fixed end condition of the test specimen can be concluded to be satisfied through the measurement of displacement at both blocks.

The transverse (radial) concentrated load is applied at the midspan by a hydraulic jack with 50 tf capacity (stroke: 200 mm). Five loading programs are presented in the

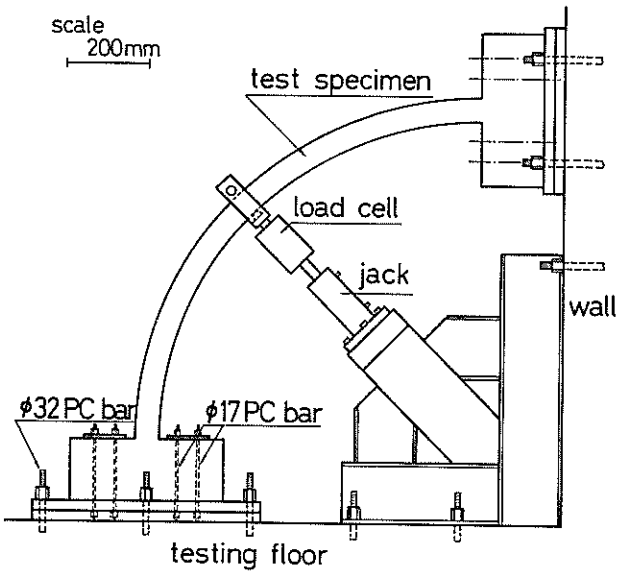

Fig. 11 Testing Setup (Side View)

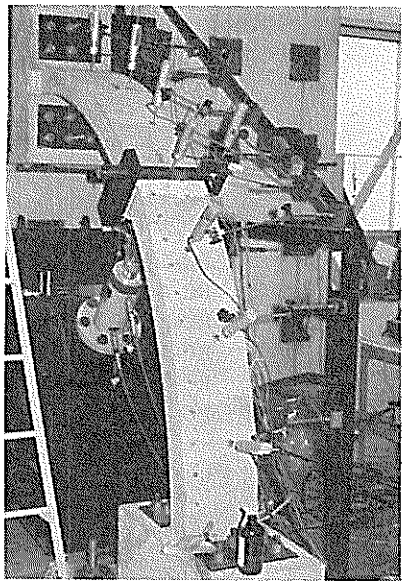

Fig. 12 General View of Testing Setup

experiment as follows:

① Monotonically increasing load is applied from the inside to the outside of the specimen.
② Monotonically increasing load is applied from the outside to the inside.
③ Repeated load is applied from the inside to the outside.
④ Repeated load is applied from the outside to the inside.
⑤ Repeated load is applied from the both sides alternately.

The loading programs of each specimen are listed in Table 10. For repeated loading ③ and ④, the load is increased by an increment of 1 tf up to the first yield of reinforcing bars. After the first yield, loading increments are controlled by the measured deflection at the midspan. Loading increments are controlled by load itself in the cases of the

Table 10 Loading Programs

No.	loading pattern	direction of loading
PC-1	monotonic	(from) outside
PC-2	monotonic	inside
PC-3	cyclic	outside
PC-4	cyclic	inside
PC-5	cyclic	both sides
RC-1	monotonic	outside
RC-2	monotonic	inside
RC-3	cyclic	outside
RC-4	cyclic	inside
RC-5	cyclic	both sides

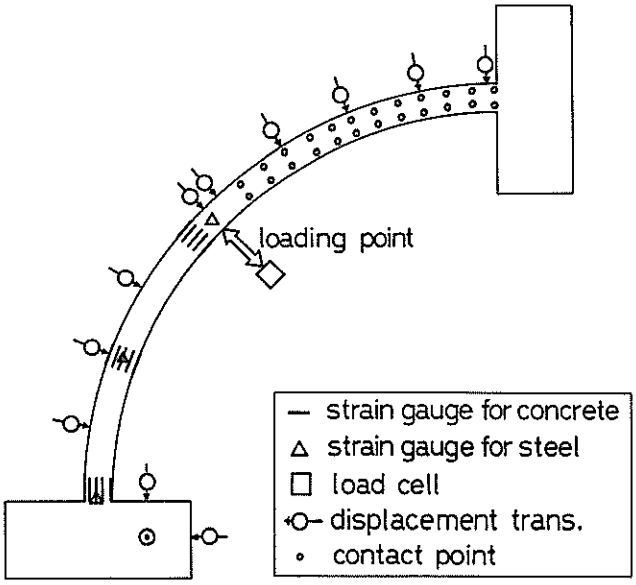

Fig. 13 Location of Instrumentation

loading programs ①, ② and ⑤. The applied load is supposed to be the wave forces, but the dynamic effects are not considered in this study.

The applied load is measured by a load cell which attached at the tip of the jack. The deflection of the test specimen is measured by displacement transducers (stroke: 50 mm). The strains in the reinforcing bars, prestressing bars and concrete are measured by electrical resistant strain gauges attached to the respective surfaces. The gauge length are 6 mm for reinforcing and prestressing bars, and 30 mm for concrete. The locations of instrumentation are shown in Fig. 13. All the transducers and gauges are monitored by a data logger through scanning boxes.

Contact points are attached on the inner and outer surface of the test specimen at the interval of 10 cm, and widths of cracks are measured by a contact type gauge. Locations of cracking, developing and so on are measured and sketched by visual inspection. Measurements are made at each loading step, and widths of cracks are measured at the maximum load in each loading cycle.

4. Experimental Results

4.1 General

The experimental results are summarized in Table 11. In this table, the loads at the ultimate condition, P_u, are defined as the maximum values in the load deflection relationships (curves). The loads at the first yield, P_y, are defined as the values when the tensile strain in the reinforcing bar reaches the yield strain obtained by the yield strength and modulus of elasticity. Loads and deflections of the specimens subjected to alternate loading (PC-5 and RC-5) listed in this table are obtained when the load is applied from the outside.

Table 11 Summary of the Experimental Results

No.	loading program	age (days)	f'_c (kgf/cm²)	f_b (kgf/cm²)	E_c (kgf/cm²)	P_u (tf)	P_y (tf)	P_c (tf)	δ_u (mm)	δ_y (mm)
PC-1	MO	134	500	77.5	—	21.0	9.8	2	8.2	3.1
PC-2	MI	117	391	56.4	2.84×10^5	11.6	4.5	2	—	2.5
PC-3	CO	264	426	58.7	2.85×10^5	20.5	9.5	2	8.8	2.7
PC-4	CI	153	412	50.0	2.96×10^5	15.2	4.5	2	46.0	3.6
PC-5	CA	268	422	63.4	2.86×10^5	16.0	10.0	2	5.5	2.7
RC-1	MO	141	472	66.4	2.79×10^5	13.0	5.8	2	8.4	2.9
RC-2	MI	134	508	66.7	2.98×10^5	6.2	2.9	1	33.6	2.6
RC-3	CO	146	438	46.8	2.86×10^5	14.7	5.9	1	13.8	4.6
RC-4	CI	171	395	54.4	2.96×10^5	7.4	2.6	1	44.8	3.2
RC-5	CA	266	420	61.4	2.94×10^5	15.1	5.0	1	9.2	2.0

M : monotonic O : from outside A : from both sides
C : cyclic I : from inside alternately

Strengths of concrete are measured at loading tests conformed to JIS A 1108 ($\phi10\times20$ cm cylinder) and JIS A 1106 ($10\times10\times40$ cm prism).

4.2 Strength and Deflection

Load-deflection curves of the specimens under each loading are shown in Figs. 14 to 23. Comparing the curves when mononotically increasing load is applied with the curves when the cyclic load is applied, the backbone curves are almost the same each other. The first yield load and ultimate load of the PC and RC specimens when load is applied

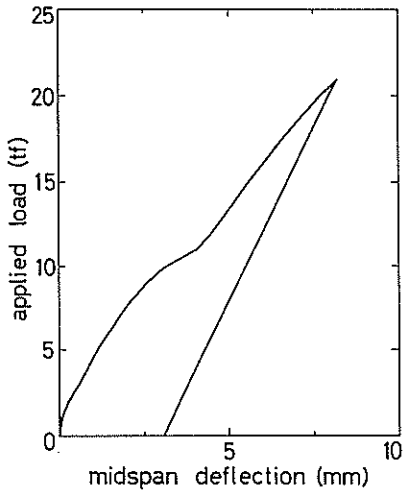

Fig. 14 Load-Deflection Curve of PC-1 (PC-MO)

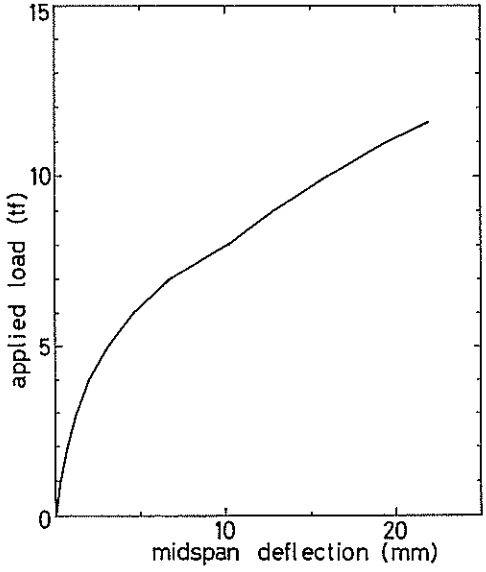

Fig. 15 Load-Deflection Curve of PC-2 (PC-MI)

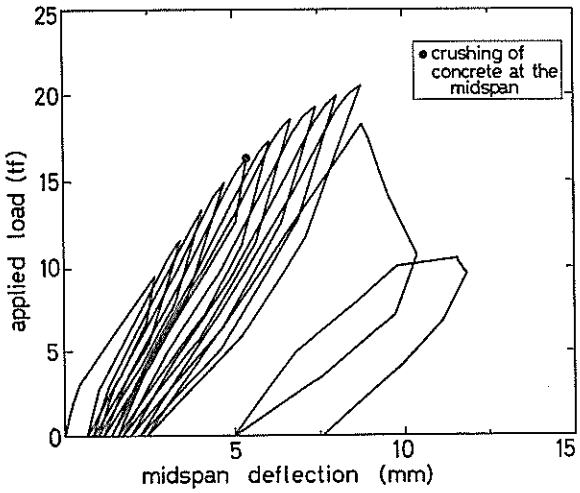

Fig. 16 Load-Deflection Curve of PC-3 (PC-CO)

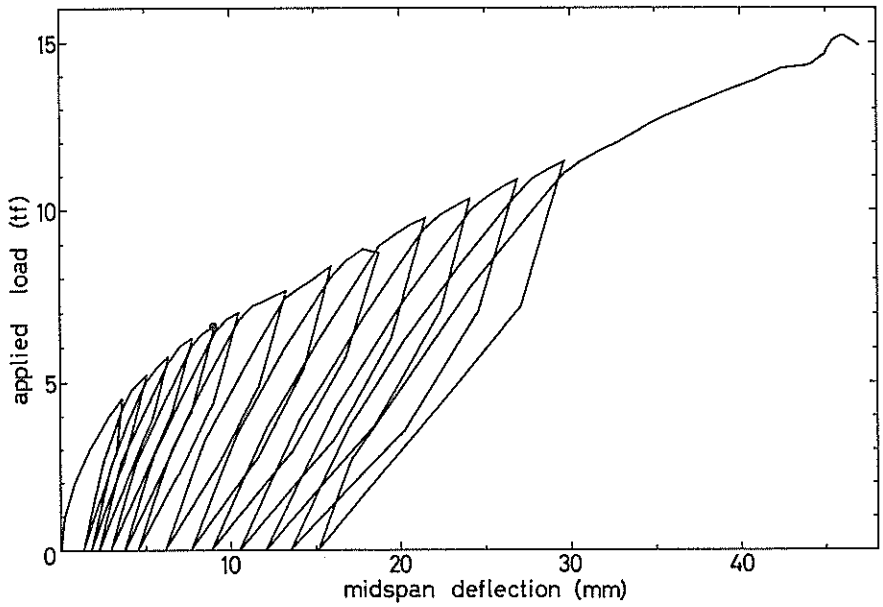

Fig. 17 Load-Deflection Curve of PC-4 (PC-CI)

from the outside are considerably larger than those when load is applied from the inside. In the RC specimens, the ultimate load when load is applied from the outside is about two times as large as that when load is applied from the inside. The first yield loads show the same results as those of the ultimate loads. In the PC specimens, the ultimate load when load is applied from the outside is about 1.4 times as large as that when load is applied from the inside. The difference of the ultimate loads depends on the direc-

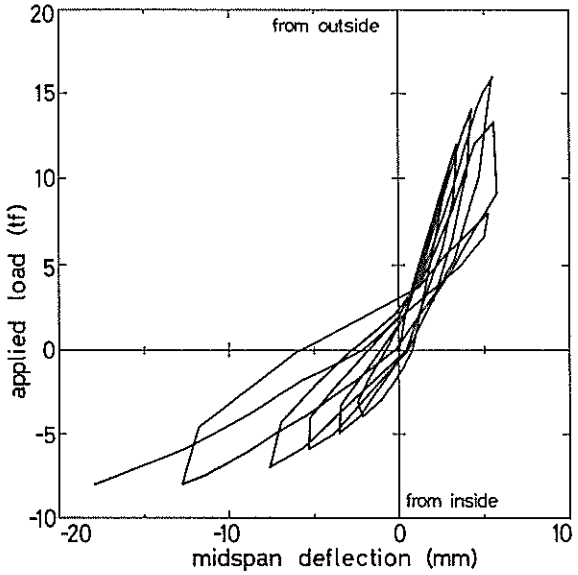

Fig. 18 Load-Deflection Curve of PC-5 (PC-CA)

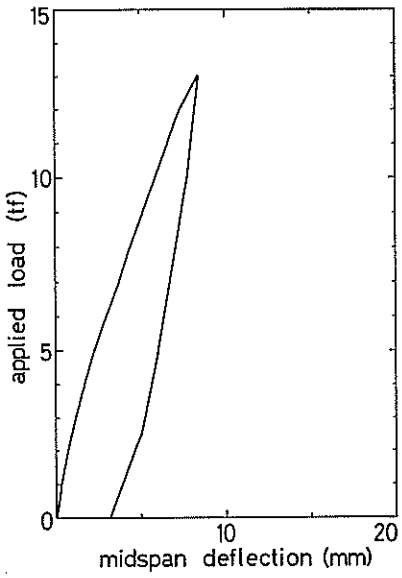

Fig. 19 Load-Deflection Curve of RC-1 (RC-MO)

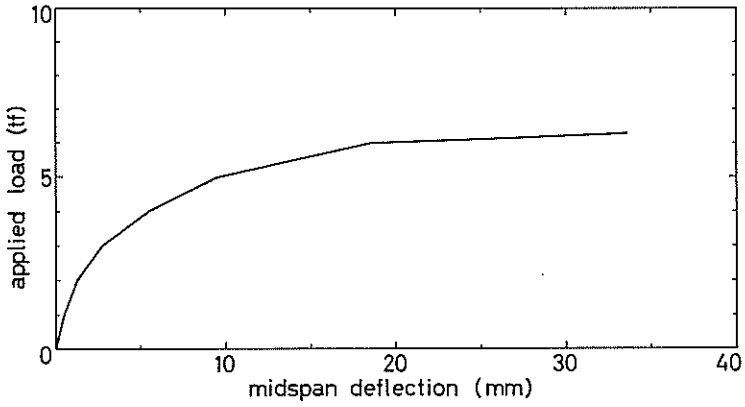

Fig. 20 Load-Deflection Curve of RC-2 (RC-MI)

tion of loading, and the direction gives more effects to the RC specimens. On the other hand, there is little difference of the first cracking load.

When load is applied from the outside, the slope of the envelope in the load-deflection curve is roughly constant up to the ultimate load. Moreover, the load-deflection curve has the conspicuous peak. The specimens provide less deflection after first yields and then collapse rapidly. On the other hand, when load is applied from the inside, the slope of envelope in the load-deflection curve gradually becomes gentler as the load is increased. Moreover, the conspicuous peak does not appear and the deflec-

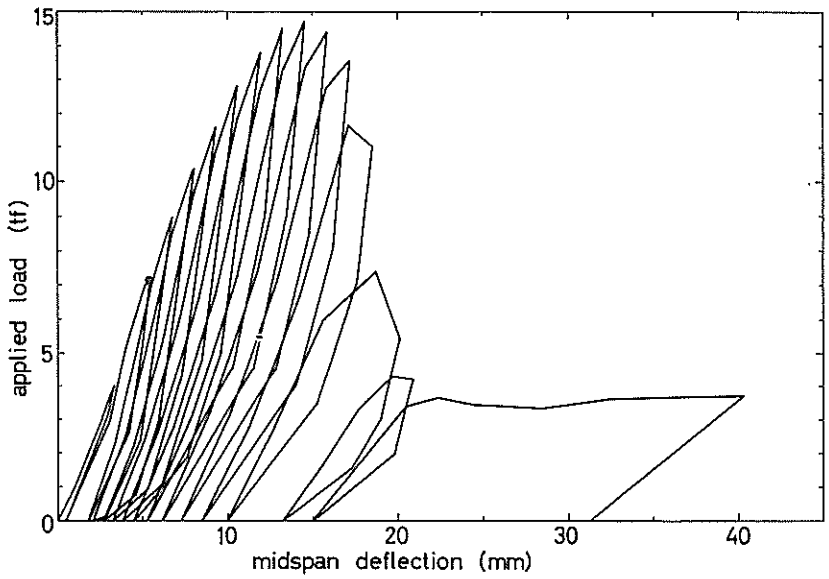

Fig. 21 Load-Deflection Curve of RC-3 (RC-CO)

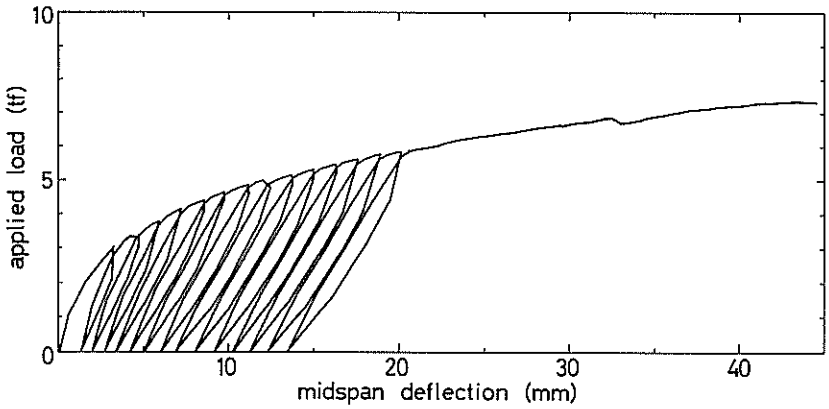

Fig. 22 Load-Deflection Curve of RC-4 (RC-CI)

tion of the specimen increases. The stiffness of the specimen keeps almost the constant value.

The load-deflection relationships for the alternate loading are almost similar to the results to be obtained by compounding the relationships when load is applied from the outside and those when load is applied from the inside.

Loads at the formation of a plastic hinge at the midspan are shown in Figs. 16, 17 and 21. The formation of a plastic hinge is defined when cracks pass through the section and crushing of the concrete is observed on the surface of the members. At this time, though the reinforcing bars already yield, prestressing bars do not yield yet in the PC specimens. Consequently, the midspan section where a plastic hinge is formed

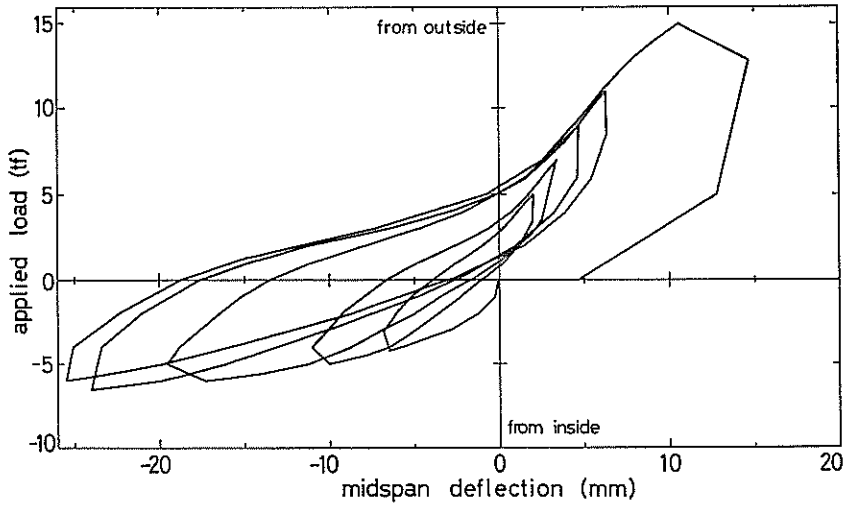

Fig. 23 Load-Deflection Curve of RC-5 (RC-CA)

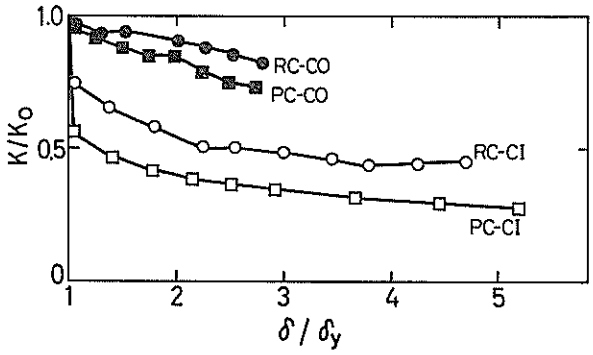

Fig. 24 Stiffness Deterioration

still has the capability of resisting the force because of prestressing bars. Namely, a plastic hinge is not formed at the midspan section in the strict sense of the words.

Figure 24 shows the ratio of average stiffness at each loading cycle to the initial stiffness plotted against the ductility factor. The average stiffness (K) is obtained by $K=dP/d\delta$ of the load(P)-deflection (δ) curves at each loading cycle. The stiffnesses of the PC and RC specimens descend with the increase in the ductility factors. The stiffness deterioration of the specimens when load is applied from the inside is greater than those when load is applied from the outside.

Figure 25 shows the deflected shapes of the PC specimens at certain load steps, and Fig. 26 shows those of the RC specimens. The deflections at the midspan obtained from the experiment are larger than those from the elastic analysis, but the deflections at the quarter span from the experiment are smaller than those from the elastic analysis when load is applied from the inside. The reason is considered that the specimens turn into two cantilevers after cracks passed through some sections near the midspan.

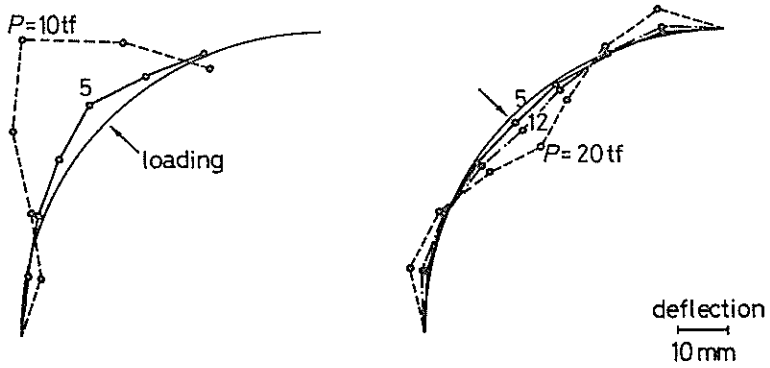

Fig. 25 Deflected Shapes of the PC Specimens

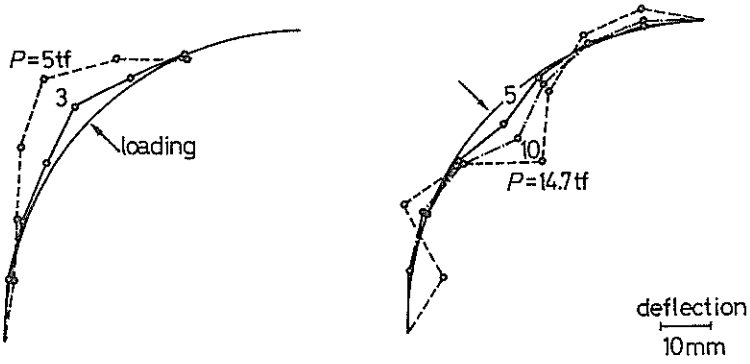

Fig. 26 Deflected Shapes of the RC Specimens

When load is applied from the outside, plastic hinges are formed at the midspan and the quarter span after the cruching of concrete. Consequently, the deflections of the specimen become different from those in early load steps.

4.3 Strains in Bars and Concrete

Figure 27 to 30 show the load-strain curves up to the yield strain in reinforcing bars at the midspan when load is applied from the outside. Tensile strain occurs and increases in the inner reinforcing bar as the load is increased. In the outer reinforcing bar of the RC specimens, though compressive strain occurs in early load steps (up to about 5 tf), tensile strain conversely occurs and increases up to about 12 tf. The strain at the maximum load in each load step for cyclic loading decreases when the applied load is beyond 12 tf. As the load is further increased, the compressive strain occurs. Residual strain (the value at taking a load off) is in the tensile state, and the value becomes larger as the loading steps are increased.

In the outer reinforcing bar of the PC specimens, compressive strain occurs and increases as the load is increased, without changing into the tensile state. In the RC specimens, however, flexural or shear cracks are initiated and propagate rapidly to the inner fiber of the concrete. Thus, the neutral axis moves outward, and results in giving

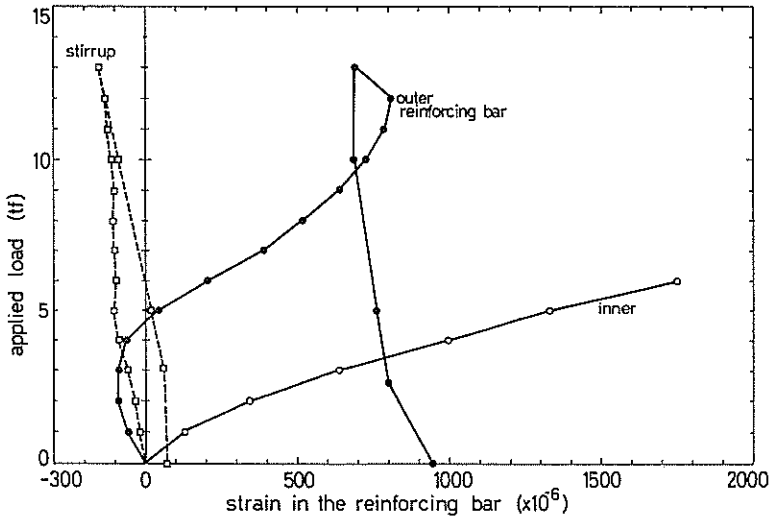

Fig. 27 Load-Strain Curves in the Reinforcing Bars (RC-MO)

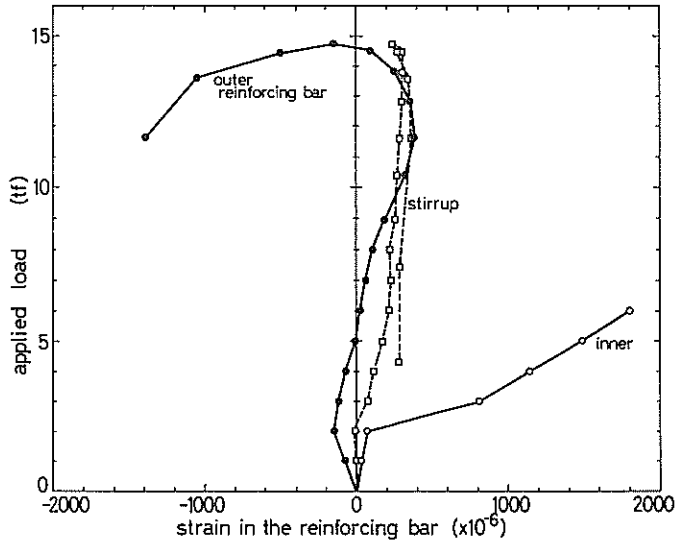

Fig. 28 Envelopes of Load-Strain Curves in the Reinforcing bars (RC-CO)

the outer reinforcing bar the tensile strain. In the PC specimen, however, prestressing stress restricts the formations and propagations of cracks. Thus, the outer reinforcing bar in the PC specimen has only compressive strain.

Figure 31 to 34 show the load-strain curves in the reinforcing bars at the midspan when load is applied from the inside. Both the outer and inner reinforcing bars are given tensile strains in the RC and PC specimens. When load is applied from the inside, tensile axial stress occurs, and has greater effect on the distribution of strain in a section than

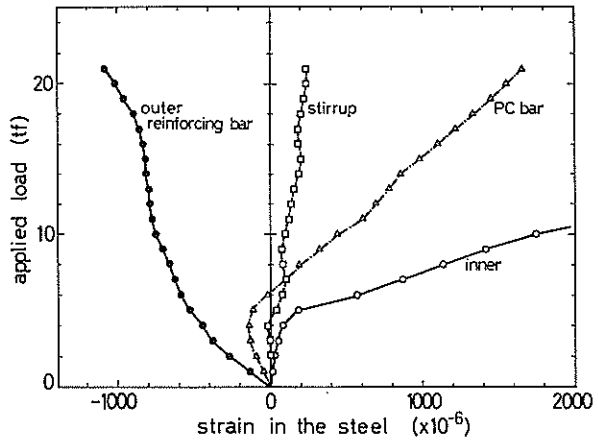

Fig. 29 Load-Strain Curves in the Steel (PC-MO)

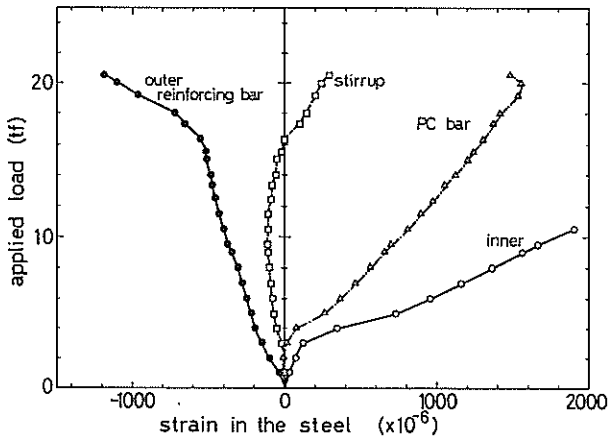

Fig. 30 Envelopes of Load-Strain Curves in the Steel (PC-CO)

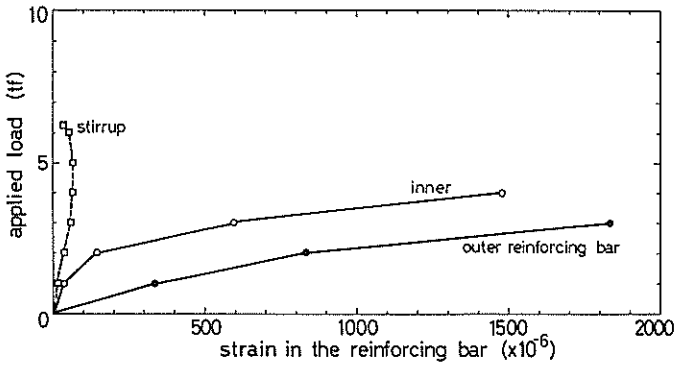

Fig. 31 Load-Strain Curves in the Reinforcing Bars (RC-MI)

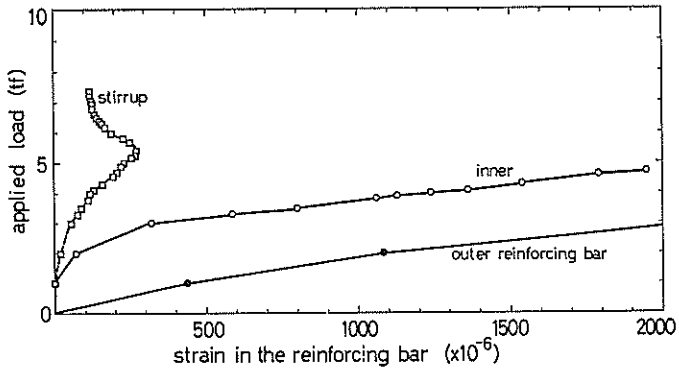

Fig. 32 Envelopes of Load-Strain Curves in the Reinforcing Bars (RC-CI)

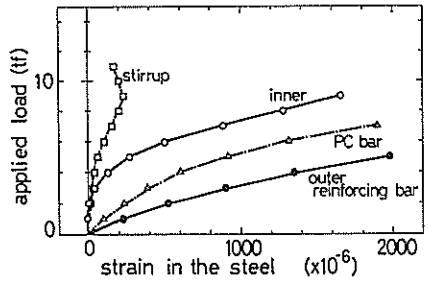

Fig. 33 Load-Strain Curves in the Steel (PC-MI)

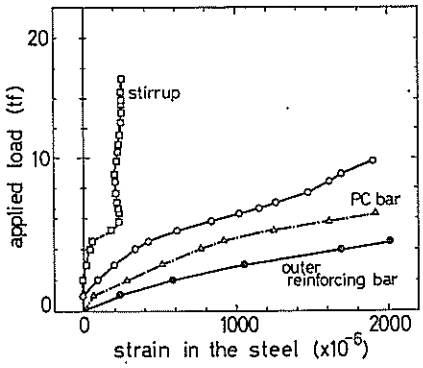

Fig. 34 Envelopes of Load-Strain Curves in the Steel (PC-CI)

flexural stress does.

Figure 29, 30, 33 and 34 show the load-strain curves in the prestressing bars at the midspan. The strain is defined as the average value occurred in two prestressing bars. Tensile strain occurs and increases both when load is applied from the outside and when load is applied from the inside.

Figure 35 shows the distribution of strain in the concrete at the midspan section when load is applied from the outside. The distribution is almost linear along the height of the section, and is not affected by the curvature of the member. The intersecting point between the distribution and the normal line move little.

4.4 Ductility and Energy Dissipated

Ductility factors at the ultimate of the specimens are listed in Table 12. The ductility factor is defined as the ratio of the midspan deflection at a certain load to that at the first yield. Namely, the ductility factor at the ultimate means the ratio of the deflection at the ultimate and that at the first yield. The ductility factors are about 6.0 when load is applied from the outside to the inside both for the PC and RC specimens. On the other hand, the ductility factors are about 13 when load is applied from

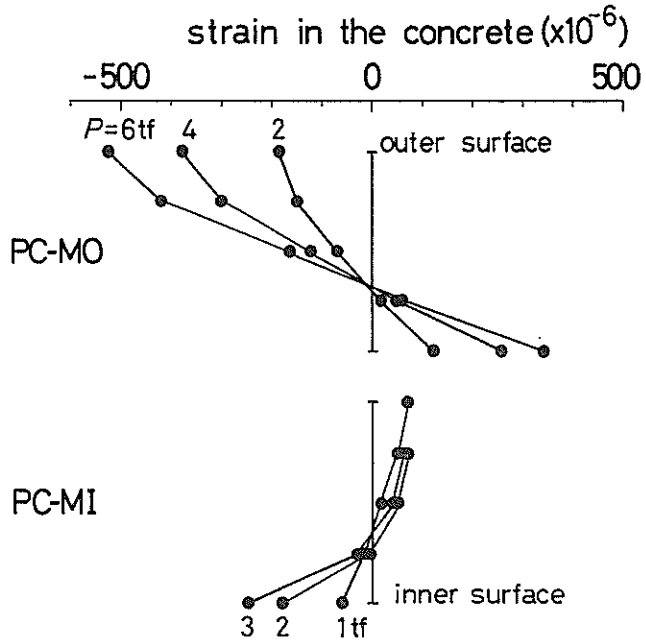

Fig. 35 Strain Distribution in the Concrete at the Midspan

Table 12 Ductility Factor at Ultimate

No.	ductility factor
PC-1	2.7
PC-2	—
PC-3	3.2
PC-4	12.8
PC-5	2.0
RC-1	2.9
RC-2	12.9
RC-3	3.0
RC-4	14.0
RC-5	4.6

the inside. Thus the ductility factor when load is applied from the inside is about four times as large as that when load is applied from the outside. The ductility factor of the specimen when alternate load is applied, is almost the same as that when load is applied from the outside and/or from the inside. As mentioned above, the arc-shaped member has a capability of large deformation when load is applied from the inside.

Figure 36 shows the equivalent viscous damping coefficient, and Fig. 37 shows the cumulative energy dissipated of the RC and PC specimens plotted against numbers of loading cycles. The equivalent viscous damping coefficient (h_e) is given by Eq. (4.1).

$$h_e=\frac{1}{2\pi}\cdot\frac{W_d}{W_t} \tag{4.1}$$

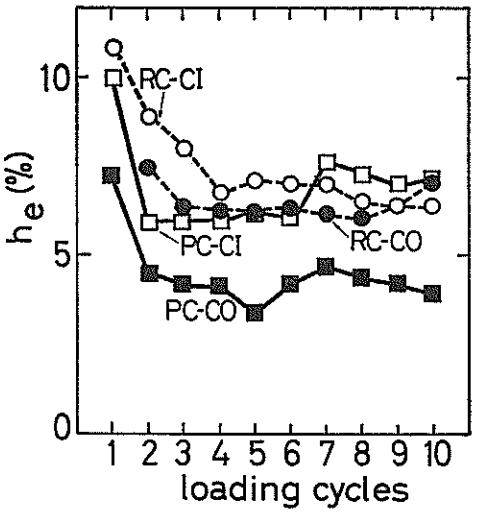

Fig. 36 Equivalent Viscous Damping Coefficient (h_e)

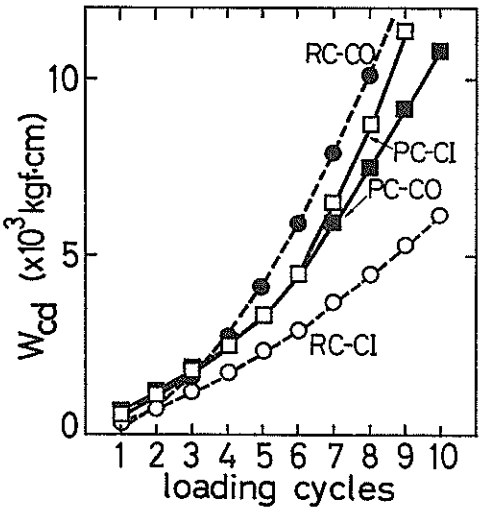

Fig. 37 Cumulative Energy Dissipated (W_{cd})

where W_d and W_i denote the dissipated and loading energy in the member, respectively. The equivalent viscous damping coefficients decrease slowly in 2 to 4 cycles of loading, and subsequently, become almost constant with the values of 4 to 6%. The direction of loading has little effect on the equivalent viscous damping coefficient of the arc-shaped member.

The cumulative energy dissipated in the RC and PC members when load is applied from the outside is about twice as large as that when load is applied from the inside. However, the difference of directions of loadings does not affect the energy dissipation in the PC members.

4.5 Crack Formation

The appearances of the members at the ultimate loads are shown in Figs. 38 and 39. Cracks are initiated in some sections near the midspan at first when load is applied from the inside, and tend to pass through the sections before other sections have cracks. After that, cracks are formed on the inner surface of concrete, widened and gradually propagate towards the outside fiber as the load is increased, and the beams subsequently turn into two cantilevers as mentioned before. Just before the ultimate load, crushing of concrete occurs at the quarter span section. The mode of failure of the member when load is applied from the inside is the flexural failure.

When load is applied from the outside, cracks are formed not only on the inner surface of concrete near the midspan section, but also at the quarter span sections at early loading stages. Cracks formed in these sections are widened and extended as the load is increased. The mode of failure of the beam is the crushing of concrete at the quarter span sections and shear failure of concrete at the midspan. Flexural moments at the midspan and at the ends of the member are almost the same as those obtained from elastic analyses. However, apparent cracks are not observed actually at the ends of the beams. The reason is considered that the flexural moment is redistributed between

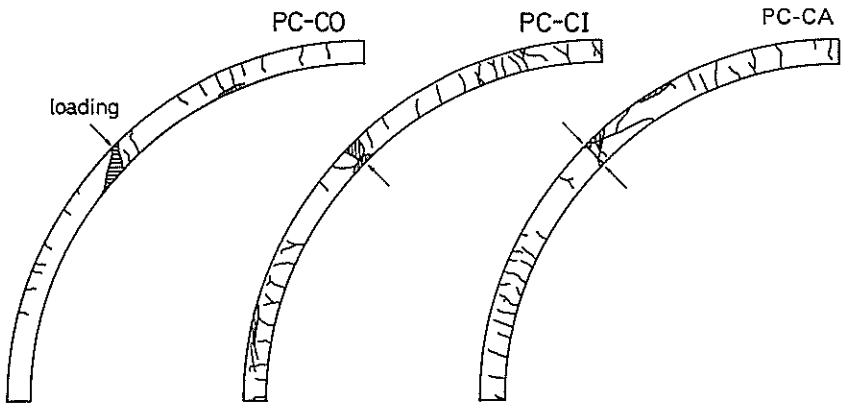

Fig. 38 Crack Formation in the PC Specimens at Ultimate

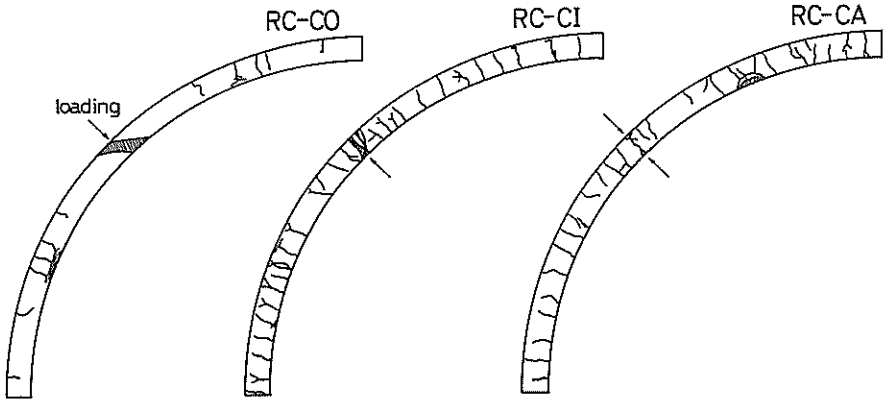

Fig. 39 Crack Formation in the RC Specimens at Ultimate

the quarter span sections after plastic hinges were developed at the midspan section.

Figure 40 shows the relationship between the applied load and the maximum width of crack at the quarter span section in the RC beams. The maximum width of crack is observed at the loading section, that is, the midspan section. An allowable width of crack in offshore structures is 0.2 mm from the viewpoint of durability. The applied loads at the maximum widths of cracks of 0.2 mm are listed in Table 13. At the same applied loads, the maximum width of crack in the members when load is applied from the outside is apparently larger than that when load is applied from the inside.

Relationship between the maximum width of crack and strain in the tensile reinforcing bar is shown in Fig. 41. The maximum width of crack is in proportion to strain in the tensile reinforcing bar up to the strain of 1000×10^{-6} when load is applied from the outside. The maximum width of crack is in proportion to strain in the tensile reinforcing bar within the limitation in Fig. 41 when load is applied from the inside. Those results are mainly due to the modes of failures. When load is applied from the

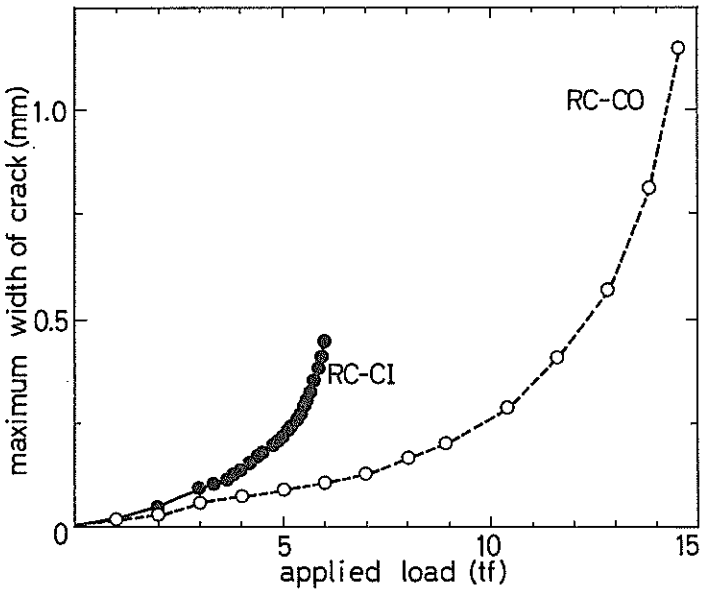

Fig. 40 Relationship between the Maximum Width of Crack and Applied Load

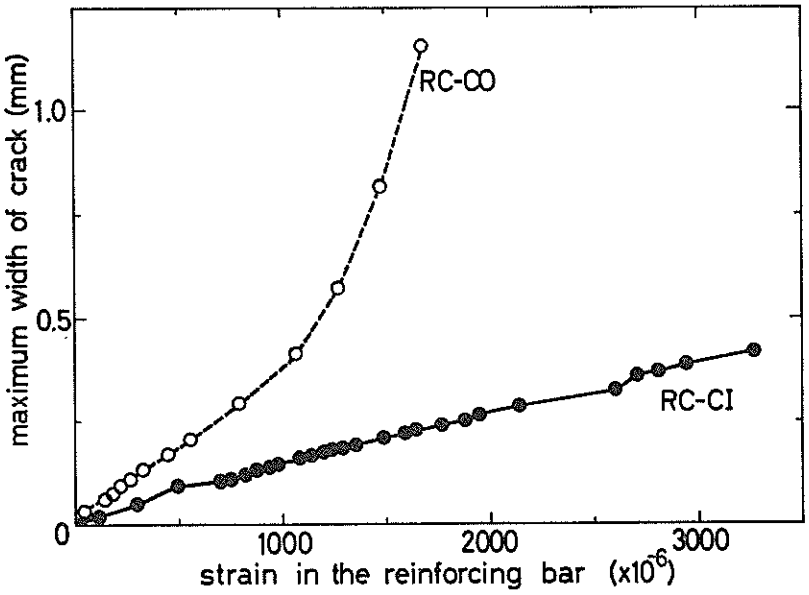

Fig. 41 Relationship between the Maximum Width of Crack and Strain in the Reinforcing Bar

Table 13 Load when the Maximum Crack Width Reaches 0.2 mm

No.	load (tf)
PC-1	—
PC-2	6.0
PC-3	12.0
PC-4	4.0
PC-5	—
RC-1	10.0
RC-2	2.0
RC-3	8.9
RC-4	1.8
RC-5	3.0

outside, plastic hinges are formed at the quarter span sections derived from the redistribution of the flexural moment, and larger width of cracks are formed as the results of the rotation in these sections. Differences between the maximum widths of cracks may be the result that strain distribution in these sections are not linear owing to the curvature of the members.

4.6 Fracture Process

Through the experimental results, the fracture process of the arc-shaped members can be described as follows:

① When load is applied from the inside.

Great cracks are formed and propagate at the midspan and then the crushing of concrete occurs. After that, a plastic hinge is formed at the midspan, and deformation and rotation concentrate there. Other sections have flexural cracks as the load is increased, but the loading energy is mostly dissipated in the plastic hinge at the midspan. Afterward tensile fracture of reinforcing/prestressing bars occur, and the member turns into two cantilever beams.

② When load is applied from the outside.

Cracks are initiated at the midspan and the quarter span. Cracks are widened and propagate in these sections, and other sections have no evident cracks. The crushing of concrete occurs at the midspan at first, and a plastic hinge is formed. After that, concrete at the midspan section is crushed. Being near at the ultimate, the midspan sections have plastic hinges, and then the member is fractured. The midspan section has shear cracks also.

5. Comparison between the Experimental Results and the Calculated Results by the Limit State Design

5.1 General

The experimental results of strengths and crack widths are compared with the calculated results obtained by formulae presented in the limit state design method. The limit state design method has been suggested by JSCE[9]. In the comparison between the experimental results and the calculated results, the load factor and the material

factor are assumed to be 1.0, that is, characteristics loads and characteristics strengths are used.

5.2 Flexure and Shear Strength

Figures 42 and 43 are the interaction diagrams of the bending moment and axial force for the PC and RC specimens. These diagrams are obtained by the limit state design method. There is little difference between the diagram for the PC specimen and that for the RC specimen beyond about 45 tf of the axial force. Figure 44 shows the distribution of bending moment calculated by the elastic analysis. In the test specimens,the axial force (N_c) and bending moment (M_c) occurred at the midspan are presented as follows:

$$\left.\begin{aligned} N_c &= 1.127P \quad \text{(tf)} \\ M_c &= 0.119P \quad \text{(tf·m)} \end{aligned}\right\} \tag{5.1}$$

where P denotes the concentrated external load.

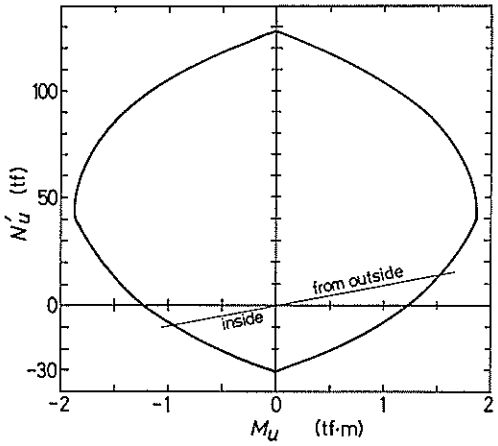

Fig. 42 Interaction Diagram of the PC Specimen

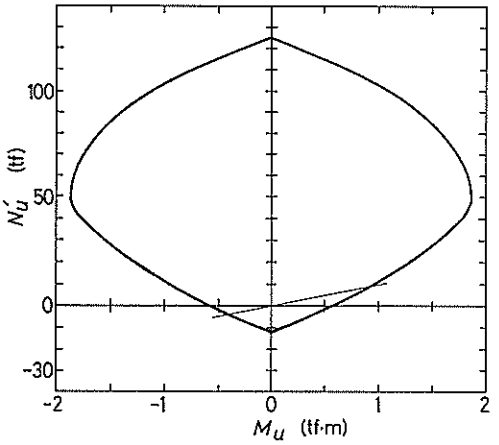

Fig. 43 Interaction Diagram of the RC Specimen

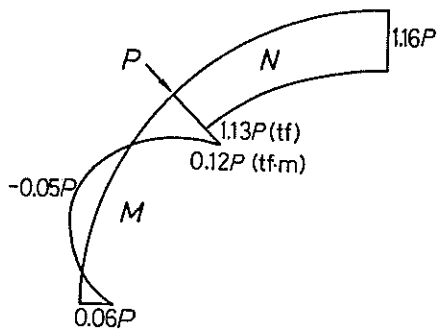

Fig. 44 Bending Moment and Axial Force Diagram

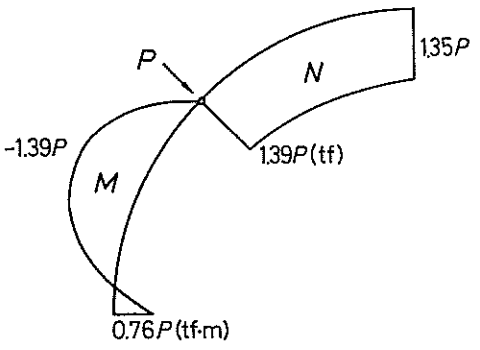

Fig. 45 Bending Moment and Axial Force Diagram

These relationships and the interaction diagrams can give the bending moment of resistance of the test specimen as follows:

(a) the PC specimen when load is applied from the outside ..... 1.48 tf·m
(b) the PC specimen when load is applied from the inside ..... 0.86 tf·m
(c) the RC specimen when load is applied from the outside ..... 0.89 tf·m
(d) the RC specimen when load is applied from the inside ..... 0.41 tf·m

The predicted applied loads for these cases at the ultimate are calculated as follows:

(a) 12.44 tf
(b) 7.23 tf
(c) 7.48 tf
(d) 3.45 tf

The experimental ultimate loads (loads at the fracturing of the member listed in Table 11) are about 1.6 to 2.1 times as large as these calculated loads. These differences can be explained by the following reasons. When the bending moment at the midspan section of the specimen reaches the ultimate value, the specimen does not collapse because of the statically indeterminacy of the member. Namely, the excess bending moment at the midspan is distributed to the other sections in the member. In the experimental work, the fracture of the test specimen occurs at the formation of plastic hinges at the midspan and the quarter spans. These predicted ultimate loads are the values when a plastic hinge occurs at the midspan, and these loads and the experimental plastic hinge formation loads at the midspan show good agreement. Consequently, it is necessary to consider the formation of plastic hinges at the quarter span for the precise estimation of the ultimate load of the member. Namely, the plastic hinges in the member are required to predict the ultimate strength for the member of the statically indeterminacy. The ultimate load must be calculated by plastic design methods. However, as the calculation method of plastic design is very difficult, it is calculated by an easier method as follows.

The distribution of bending moment is calculated when the midspan section does not transmit the bending moment. Figure 45 shows the distribution of the bending moment. Through Figs. 44 and 45, the ultimate bending moment at the quarter span is obtained by adding both values of bending moments. As the result of that, the fracture loads of the test specimens are calculated as follows:

(a) 19.35 tf
(b) 11.57 tf
(c) 11.82 tf
(d) 5.27 tf

The experimental ultimate loads are 1.1 to 1.2 times as large as these calculated ultimate loads. Consequently, the strength of the arc-shaped member is predicted fairly well by the structural analysis in consideration of the formation of plastic hinges and distribution of the bending moment, and by the limit state design method.

The shear strength of the specimen (V_d) can be calculated in Eq. (5.2) presented in the limit state design method[9].

$$\left.\begin{aligned} V_d &= V_{cd} + V_{yd} \\ V_{cd} &= f_{vd} \cdot b_w \cdot d / \gamma_b \\ V_{yd} &= A_w \cdot f_{wyd} \cdot z(\sin\alpha + \cos\alpha)/s/\gamma_b \\ f_{vd} &= f_{vod}(1 + \beta_d + \beta_p + \beta_n) \\ f_{vod} &= 0.94 \sqrt[3]{f'_{ck}}/\gamma_c \end{aligned}\right\} \qquad (5.2)$$

$$\left.\begin{aligned}&\beta_d=\sqrt[4]{100/d}-1\geqq 1 \quad (d\text{: cm})\\&\beta_p=\sqrt{100p_w}-1\leqq 0.73\\&\beta_n=M_0/M_d\leqq 1\end{aligned}\right\}$$

where b_w: the width of the member, A_w: the area of web reinforcement, f_{wyd}: the design yield strength of web reinforcement, s: the spacing of web reinforcement, p_w: the reinforcement ratio, M_0: the bending moment at the decompression and M_d: the design bending moment of resistance. The calculated shear strengths (resisting loads) are as follows:

(a) 14.04 tf
(b) 15.02 tf
(c) 14.14 tf
(d) 15.16 tf

The ultimate shear strengths are larger than the ultimate flexure strengths except the case (a). In the case (a) (the PC specimen when load is applied from the outside), the load at the shear failure is larger than that at the formation of a plastic hinge at the midspan. Namely, after a plastic hinge is formed at the midspan, the shear failure occurs at the midspan. Further as the load is increased, plastic hinges are formed at the quarter span, and then the member fractures. These results are in accordance with the experimental results.

5.3 Crack Width

Several formulae regarding the crack width have been proposed. Two formulae are adopted in this study. One is proposed by the limit state design in JSCE as presented in Eq. (2.6). This formula is a modified version of the formula proposed by Gergely and Lutz. The other is proposed by CEB-FIP in 1978[15], which is applied to offshore structures widely. The applicability of the above two formulae to the arc-shaped member is examined.

The proposed formula by CEB-FIP is expressed as follows:

$$\left.\begin{aligned}&w_k=1.7w_m\\&w_m=S_{rm}\cdot\varepsilon_{sm}\\&S_{rm}=2\left(c+\frac{c_\phi}{10}\right)+k_1k_2\frac{\phi}{\rho_r}\\&\rho_r=A_s/A_{c,ef}\\&\varepsilon_{sm}=\frac{\Delta\sigma_s}{E_s}\left[1-\beta_1\beta_2\left(\frac{\Delta\sigma_{sr}}{\Delta\sigma_s}\right)^2\right]\geqq 0.4\frac{\Delta\sigma_s}{E_s}\end{aligned}\right\} \qquad (5.3)$$

where w_k denotes the characteristic crack width.

Figure 46 shows the calculated crack widths of the RC specimens. Both formulae give the values of crack width greater than the experimental results, when load is applied from the outside or when load is applied from the inside up to the yield of reinforcing bars; it may be said that the calculation is on the safe side for the structural design. These formulae for crack width are applied to flexural cracks. However, they cannot give the precise widths of shear cracks and concentrated cracks. When load is applied from the outside, concentrated cracks are observed at the midspan and the quarter span sections as the load is increased. Consequently, these formulae are inapplicable to the arc-shaped member when the applied load is increased. The allowable crack width

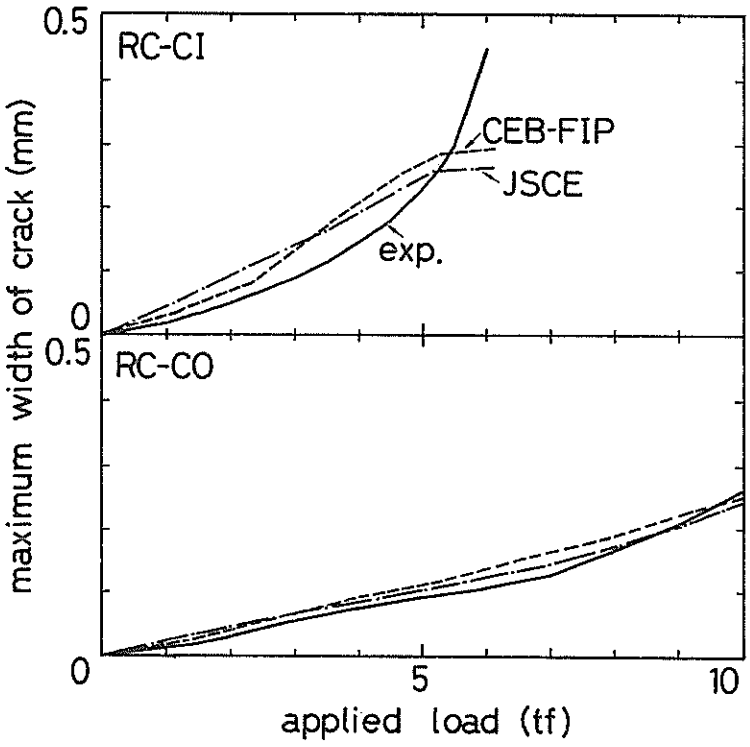

Fig. 46 The Experimental and Calculated Width of Crack

in offshore structures are determined as the function of the concrete cover. In ordinary offshore structures, the allowable crack width is calculated up to 0.2 mm. Although both formulae for crack widths give smaller values than the experimental values when the load is increased near at the ultimate, the crack width up to 0.2 mm is predicted fairly well or on the safe side by both formulae.

5.4 Discussion

Through the comparison between the experimental results and the calculated results by the limit state design, the design method of the arc-shaped member is suggested as follows. The bending moment, the axial force and the shear force must be calculated by the structural analysis in consideration of the formation of plastic hinges. Here the curvature of the arc-shaped member is to be taken into account in the structural analysis to estimate the bending moment and the axial force. The flexural and shear strength in a section of the member can be calculated by the ordinary limit state design method. When a curvature index (described in **1.2**) is greater than 0.2, the effect of the curvature should be considered. When a curvature indes does not exceed 0.2, however, the strength in a section of the member can be obtained as straight members.

The width of crack in the arc-shaped member becomes great after plastic hinges are formed. In the investigation for the serviceability limit state of the arc-shaped mem-

ber (the maximum crack width does not exceed about 0.2 mm), formulae for predicting crack widths give the values on the safe side.

6. Numerical Analysis by the Finite Element Method

6.1 General

One of the most effective methods for predicting and evaluating the mechanical properties and the fracture process of the arc-shaped member is the numerical analysis by the finite element method. The finite element method which describes nonlinear properties of concrete and steel can be applied for the numerical analysis of the arc-shaped members. The nonlinear finite element procedure currently in use is fully described elsewhere[16], and will, therefore, be discussed only briefly here. In particular, assumptions and modeling of the materials and structures, determining the various constants of materials, the accuracy of the analysis and so on were made clear in the authors' preceding paper[17]. The applicability of the analytical model in the nonlinear finite element analysis to the arc-shaped member is confirmed by comparing the analytical results with the experimental results. Further, more detailed properties of the arc-shaped member can be examined through the analysis, that is, the fracture process and the internal stress distribution can be evaluated. Geometric nonlinearities and time dependent effects are not considered in this study.

Although both PC and RC specimens are employed for the loading test, only the RC specimens under monotonically increasing loading are the subject of the numerical analysis.

6.2 Concrete Idealization

The arc-shaped member in this study can be approximated as being in a state of plane stress. Strength and stress-strain behavior of concrete must be considered under biaxial condition in modeling the member. Various models for the biaxial strength and stress-strain behavior of concrete have been proposed[18,19]. The biaxial strength envelope shown in Fig. 47 is chosen to the model in this study. Under biaxial compression, the strength envelope of concrete is determined as the Drucker-Prager yield law. Under biaxial tension, concrete has the same tensile strength as the value obtained under uniaxial loading (splitting tensile strength). Under combinations of tension and compression, the strength envelope is linear, which is defined with the uniaxial compressive and the uniaxial tensile strength (splitting tensile strength) of concrete.

As shown in Fig. 48, the stress-strain relationship of concrete is assumed to be trilinear in this study which is approximated as the experimental results. The equivalent stress relationship is assumed to be the same as the stress-strain relationship under uniaxial condition. The equivalent stress and strain can be obtained with the first and second invariants of the stress deviator tensor, J_1 and J_2.

$$J_1=\sigma_x+\sigma_y+\sigma_z \tag{6.1}$$

$$J_2=\frac{1}{6}[(\sigma_x-\sigma_y)^2+(\sigma_y-\sigma_z)^2+(\sigma_z-\sigma_x)^2]+\tau_{xy}^2+\tau_{yz}^2+\tau_{zx}^2 \tag{6.2}$$

The stress-strain relationships of concrete can be divided into three parts: before yielding, during plastic flow and after fracture (or failure). Concrete behavior before yielding is assumed to be elastic. During plastic flow, the behavior of concrete is presented by the plastic stress-strain relations. When the state of stress lies within the

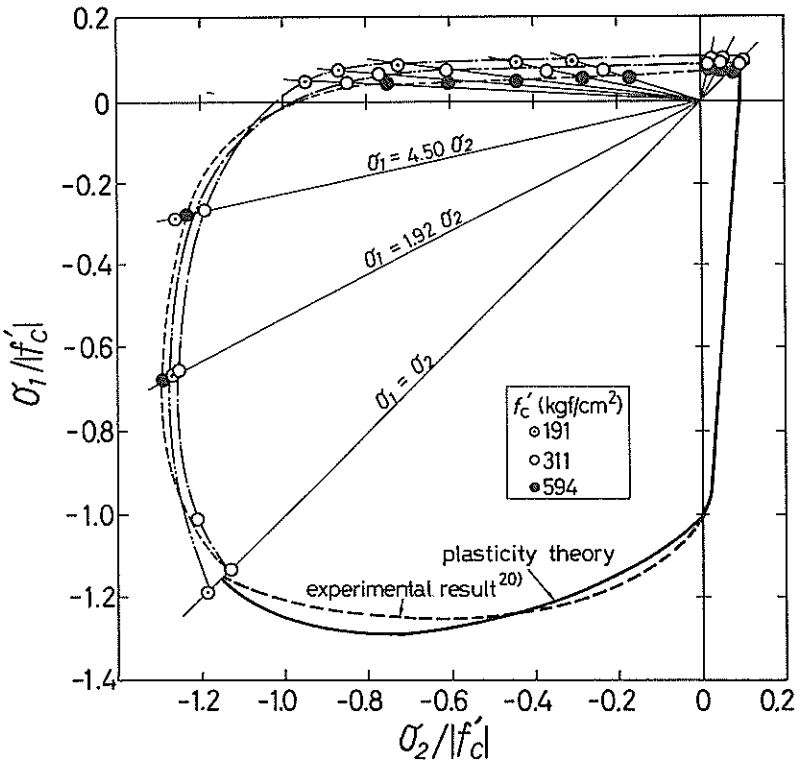

Fig. 47 Biaxial Strength Envelope of Concrete

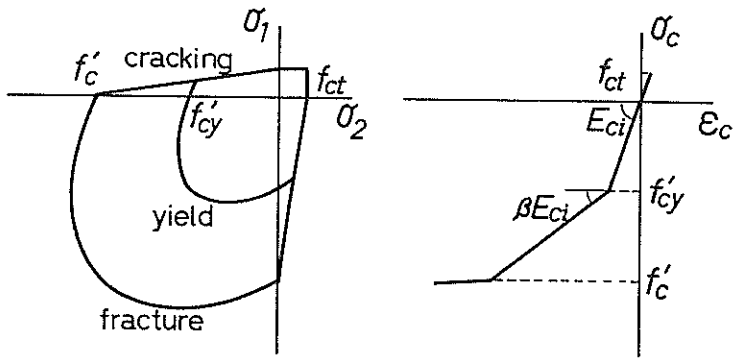

Fig. 48 Biaxial Strength Envelope and Stress-Strain Relationship of Conrete

yield surface, the concrete behavior is assumed to be in the elastic range. When the concrete stresses are beyond the elastic limit surface, a subsequent new surface is developed. The final collapse of concrete is defined when the state of stresses reaches the fracture surface and concrete crushing occurs. The formulation of the constitutive relations for concrete is based on three fundamental assumptions.

① The shape of a fracture surface is defined by the Drucker-Prager yield criterion, that is,

$$f=\alpha J_1+\sqrt{J_2}=\frac{1}{\sqrt{3}}|f_c'| \qquad (6.3)$$

α can be determined as 0.07 based on the experimental biaxial test data by Kupfer et al.[20]

② The shape of a yield surface is assumed to be similar to that of the fracture surface.

③ The formulation of the constitutive relation for concrete is the associated flow rule, that is, the direction of the plastic strain increment vector is in the direction of the normal to the current loading surface.

An isotropic hardening rule is adopted, which the initial yield surface is assumed to expand uniformly without distortion as plastic flow occurs. The function specifies the rate the of strain hardening of concrete and its shape may be defined by a uniaxial compressive stress strain curve. The strength at which the yielding of concrete occurs is determined as a half of the compressive strength (Fig. 48).

Under biaxial tension or combinations of tension and compression, a crack is assumed to be formed, as soon as the state of stress lies beyond the brittle fracture surface. Analytical modeling of concrete cracking in this study may be made by treating the gross effect of cracks distributed in a concrete element, that is, "smeared" cracking models. When a crack is formed, the tensile stress acting on the crack plane is released and redistributed to the neighboring elements. Under subsequent loading, concrete loses its tensile strength perpendicular to the crack direction, but retains the tensile strength in the directions parallel to the crack plane. The shear stress acting on the crack plane is not released but modified by the process discussed below because of the aggregate interlocking. Therefore, after the cracks have developed in a concrete element, the modified constitutive equations must be written with reference to the cracked directions. Namely, after a crack occurs, the modulus of elasticity of concrete is reduced to zero, perpendicular to the cracking direction. Moreover, the shear modulus is reduced according to crack widths, deformation of members and so on. Reduction of the shear modulus (G) is assumed to be 0.5 G in the calculation model. Models for tension stiffening in concrete after cracking is not taken into account.

6.3 Steel Idealization

Reinforcing bars are idealized with both the discrete and the distributed models. The distributed model means that reinforcing bars are assumed to be distributed over the concrete element and a composite concrete-reinforcement constitutive relation is used. Stirrups are represented with the distributed model. The bond stress between stirrups and concrete is assumed not to be released during loading. Namely, perfect bond must be assumed between concrete and stirrups in this model. A longitudinal reinforcing bar is represented with the discrete model. The longitudinal reinforcing bar can also be supposed to be in the state of plane stress. However, reinforcing bars in concrete can be considered to transfer and resist the stress of axial direction of the element. Consequently, reinforcing bars are replaced by an isotropic model and an anisotropic model. The stress-strain curves for reinforcing bars in compression are assumed to be identical to those in tension. The steel stress-strain curve may be idealized to be bilinear (elastic perfectly plastic) as shown in Fig. 49.

The yield of reinforcing bars is defined by the von Mises law. The formulation of the constitutive relation is obtained by the associated flow rule. Tensile fracture of

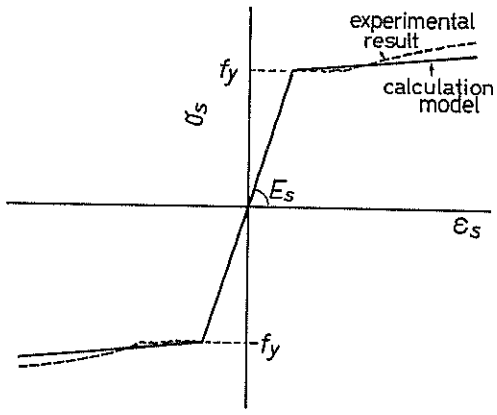

Fig. 49 Stress-Strain Relationship of Reinforcing Bar

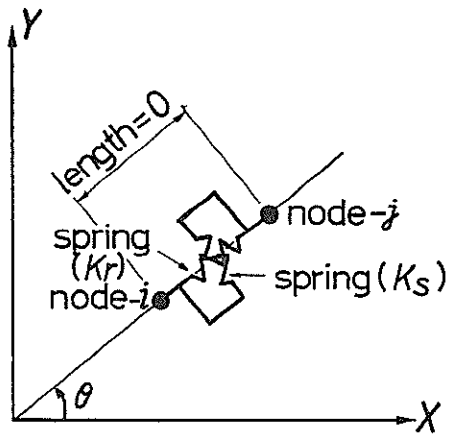

Fig. 50 Bond-Link Element

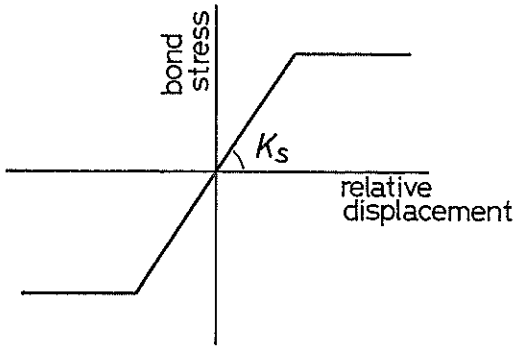

Fig. 51 Bond Stress-Relative Displacement Relationship

reinforcing bars is not considered in this model.

Bond link elements are used for modeling of the bond-slip relation. The bond link element consists of two orthogonal springs which transmit shear and normal forces between the two nodes as shown in Fig. 50. Transmitting of shear and normal forces is modeled in consideration of the dowel action and bond stress-slip relationships. The bond stress-slip relationship between concrete and reinforcing bar is assumed to be bilinear as shown in Fig. 51.

6.4 Modeling for the Arc-Shaped Member

The finite element mesh layout for the arc-shaped member employed for the experiment is shown in Fig. 52. Because of the symmetry condition, the half of the test specimen can be analyzed. The blocks fixed at the end of the specimen are not modeled into meshes. Nodes at the end of the specimen are cramped in place of meshes.

The midspan section of the test specimen (where load is applied) has evident cracks and a plastic hinge is formed after the crushing of concrete through the experimental results. Then the specimen turns into two cantilever beams. Therefore in the finite element analysis, the properties of the plastic hinge must be taken into consideration

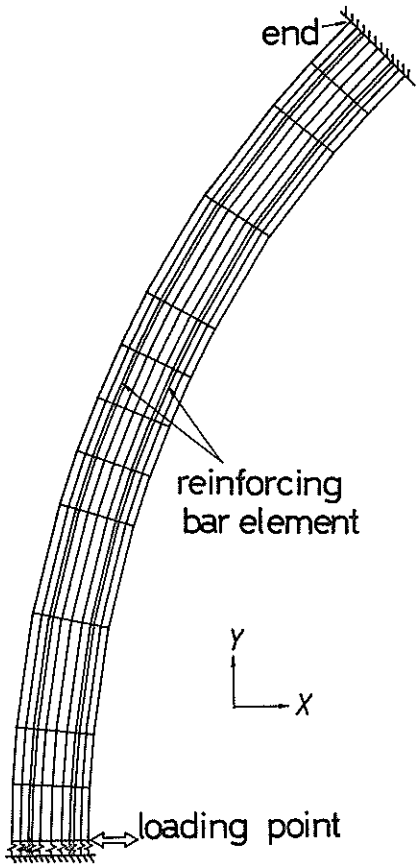

Fig. 52 Finite Element Mesh Layout

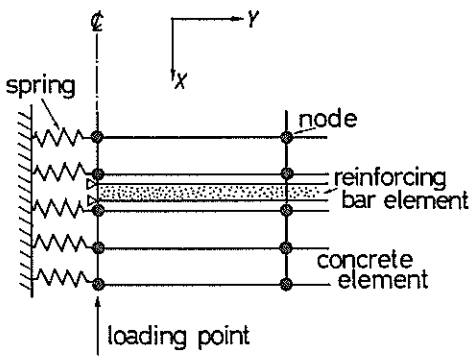

Fig. 53 Modeling near the Midspan

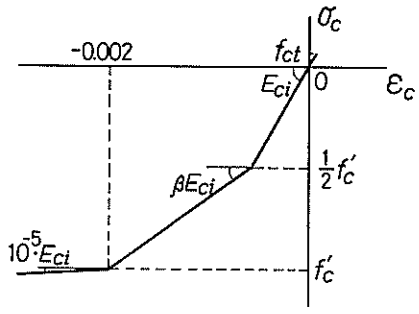

Fig. 54 Uniaxial Stress-Strain Curve of Concrete

and be modeled. A plastic hinge has an ability of rotation, and then the bending moment beyond the yield moment will be distributed. The plastic hinge is modeled by several axial springs attached to the nodes on the midspan section in this model. In the ordinary finite element analytical model for a symmetric structure in a state of plane stress, the boundary condition of the nodes on the axis of symmetry will be given by the following procedures. Nodal displacement perpendicular to the axis of symmetry is cramped, and nodal displacement parallel to the axis of symmetry is free. In the arc-shaped member, however, this symmetrical condition cannot be applied because the failure of the test specimen is likely to be affected by the modeling of the plastic hinge mentioned before.

Figure 53 shows the modeling of the midspan section in this study. Springs are connected between the node on the loaded section and the supposed node on the fixed boundary. In a state of plane stress, the rotative spring cannot be adopted in the finite element model. However, several axial springs can explain the rotation of the midspan. A spring constant is 0 or 10^{30} tf/m in case of tension or compression, respectively. Moreover in other words, the discrete cracking model is applied at the midspan, and the width of crack at the midspan can be estimated by the deformation of the spring.

Table 14 List of Material Properties

(*kgf/cm²)

loading	f'_c *	f_{ct} *	E_{ci} *	β	ν	f_y *	E_s *
from inside	508	25	2.8×10^5	0.41	0.17	3720	2.1×10^6
from outside	472	25	2.7×10^5	0.41	0.17	3720	2.1×10^6

Isoparametric rectangular plane stress elements are used for concrete and longitudinal reinforcing bars in the finite element model. The elements for reinforcing bars are overlapped with the concrete elements. Numbers of nodes and elements in this analytical model are 143 and 144, respectively. Bond-link elements are used for modeling of the bond stress-slip relationship between the concrete and reinforcing bar. Bond-link elements are installed between the nodes for the concrete and the reinforcing bar. Bond stress-slip relationship is assumed to be bilinear and the maximum bond strength is determined as 25 kgf/cm² in the calculation model. Material constants are listed in Table 14 which are obtained by the preliminary experiment.

The modelings for unloading, cyclic loading and prestressing forces are not established in the finite element analysis program in this study.

6.5 Numerical Procedure

Numerical procedures for nonlinear analysis by the finite element method are presented elsewhere in detail[21]. The flow chart for the nonlinear finite element analysis in this study is shown in Fig. 55. The analytical flow is summarized as follows:

① The material constants to be used in the constitutive equations are defined.
② The incremental strains are calculated from the increment of displacement.
③ Elastic-stress increments are calculated.
④ The yield states are checked on the basis of the stress increments. For elastic state, the elastic material matrix is formed and then go to step ⑨. For plastic state, next steps must be continued.
⑤ The fracture, crushing or cracking of concrete is checked.
⑥ The stiffness matrix of the material is formed (elastic-plastic state).
⑦ The incremental stresses are calculated by the incremental strains based on the step ⑥.
⑧ Steps ① to ⑦ are followed for reinforcing bars. Then smeared stress-strain matrix is obtained for both concrete and reinforcing bars.
⑨ The stresses and strains in the element are updated. Then go to Step ①.

The finite element analysis program in this study utilizes an incremental loading procedure for solving the nonlinear equations mentioned above. An incremental form of the constitutive relations is therefore needed, and the incremental stress ($\Delta\sigma$)-strain ($\Delta\varepsilon$) relations can be generally adopted. These relations are expressed in the following matrix form.

$$\{\Delta\sigma\}=[D^{ep}]\{\Delta\varepsilon\}-\{\sigma_0\} \tag{6.4}$$

where $[D^{ep}]$ denotes the elastic-plastic stiffness matrix.

The incremental strain is calculated by the sum of elastic strain values and the plastic incremental strain. The plastic incremental strain can be obtained using the plastic potential ($g(\sigma_{ij})$).

$$\{d\varepsilon_p\}=h\left\{\frac{\partial g}{\partial f}\right\}df \tag{6.5}$$

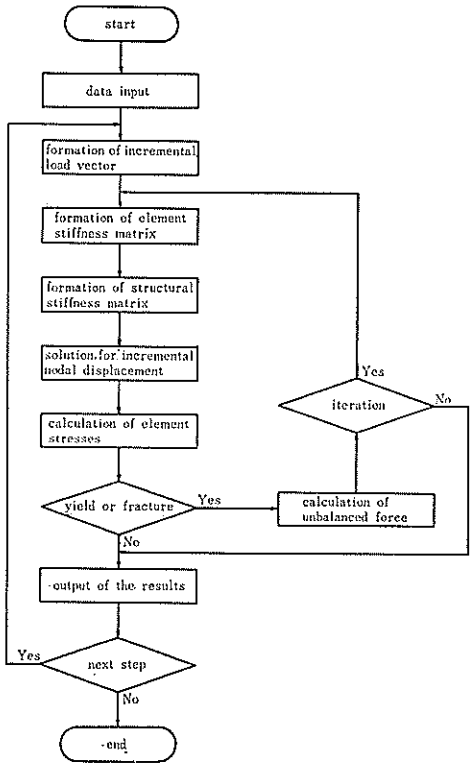

Fig. 55 Flow Chart of the Finite Element Analysis Program

When the yielding and crushing occur in the concrete element and the yielding occur in the reinforcement element, the material stiffness matrix will be corrected. On the basis of the flow rule, the corrected material stiffness matrix is obtained by Eq. (6.6).

$$[D^{ep}]=[D^e]-\frac{[D^e]\{\partial f/\partial\sigma\}\{\partial f/\partial\sigma\}^T[D^e]}{H'+\{\partial f/\partial\sigma\}^T[D^e]\{\partial f/\partial\sigma\}} \tag{6.6}$$

where H' denotes a hardening parameter. Moreover, when cracks develop in the concrete element, the above incremental equations are written with reference to the cracking directions.

For a loading increment at the steps N to $N+1$, the structural equilibrium equations can be written as follows:

$$[K]\{\Delta U\}=\{\Delta F\} \tag{6.7}$$

where $[K]$ and $\{\Delta U\}$ denote the structural stiffness matrix and the incremental nodal displacement vector, respectively. Here, $\{\sigma\}$ is the internal element stress at step N, and $[B]$ is the element strain-nodal displacement matrix. When equilibrium iterations are employed, the incremental nodal force vector $\{\Delta F\}$ may be viewed as an unbalanced nodal vector for the ith iteration cycle within the incremental loading step.

$$\{\Delta F\}_i=\{F\}_{N+1}-\sum\int_V[B]^T\{\sigma\}_{N+i}dV \tag{6.8}$$

$$i=1, 2, \cdots\cdots, m$$

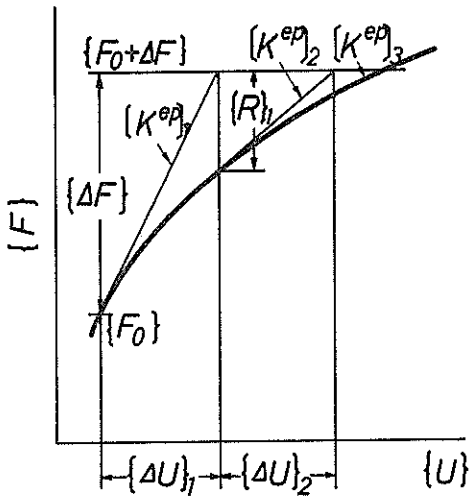

Fig. 56 The Concept of the Newton-Raphson Method

The Newton-Raphson method is applied for solving the equilibrium equations by the iteration procedure. The concept of the calculation algorithm can be figured in Fig. 56.

7. Comparison between the Experimental Results and the Calculated Results by the Finite Element Method

7.1 General

Comparison between the experimental results and the calculated results is made to confirm the applicability of the nonlinear finite element analysis to the arc-shaped member. Furthermore, the detailed behaviors of the member, in particular the fracture process of the member, can be examined and evaluated through the nonlinear analysis by FEM. The following two cases are selected in the analysis for the comparison.

① the reinforced concrete member when monotonically increasing load is applied from the outside to the inside (RC-1 in Chaps. **3** and **4**)

② the reinforced concrete member when monotonically increasing load is applied from the inside to the outside (RC-2)

The finite element analysis program in this study has been developed by the authors. An ACOS-1000 computer (NEC) at the Port and Harbour Research Institute is used in this analysis.

7.2 Strength and Deflection

Figures 57 and 58 show the computed results of the load-deflection curves for the arc-shaped member in comparison with the experimental results. When load is applied from the inside, the load-deflection relationship of the member obtained by the analysis is in accordance with that obtained by the experiment. The analytically predicted loads at the first crack, at the first yield and at the ultimate (crushing of concrete) are 1.6 tf, 3.2 tf and 7.0 tf, respectively. The experimental results of them are 1.0 tf, 3.0 tf and 6.3 tf, respectively. Both results show good agreement each other. When load

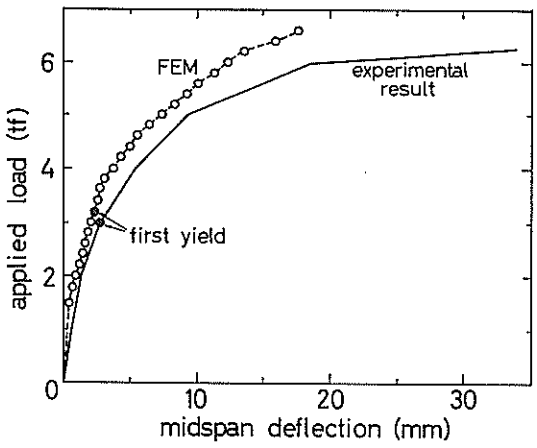

Fig. 57 The Computed and Experimental Load-Deflection Curve when Load is Applied from Inside

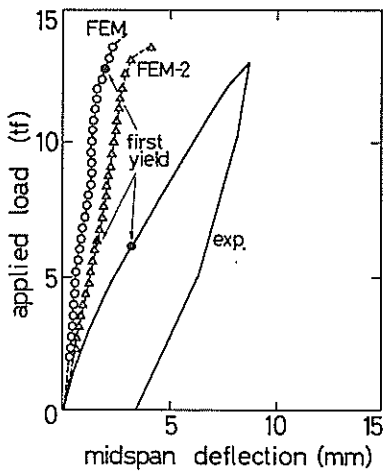

Fig. 58 The Computed and Experimental Load-Deflection Curve when Load is Applied from Outside

is applied from the outside, the computed load-deflection relationship of the member is considerably different from that of the experimental result. The analytically predicted loads at the first crack, at the first yield and at the ultimate are 3.2 tf, 12.8 tf and 18.0 tf, respectively. The experimental results of them are 2.0 tf, 6.2 tf and 13.0 tf. In particular, the analytical load at the first yield is about two times as large as that of the experimental result. These differences may be resulted from the constitutive model for the reinforcing bar elements. Namely, the mechanism of resisting and transmitting stresses in reinforcing bars are related to the strength of the arc-shaped member. Therefore, the constitutive model for reinforcing bars in the analysis described in **6.3** has been modified so that the model is capable of transmitting the axial force only. The new model is designated as FEM-2. The computed load-deflection relationship obtained by FEM-2 is also shown in Fig. 58. Although the computed load-deflection curve comes downward compared with that of the ordinary isotropic model, the computed and the experimental results still do not correspond. The analytically predicted loads by FEM-2 are 2.8 tf at the first crack, 6.2 tf at the first yield and 14.4 tf at the ultimate. These analytical loads, in particular the load at the first yield, show good agreement with those of the experimental results. The difference between the computed deflection and the experimental deflection at the same load is resulted from the formation of plastic hinges, whose rotative abilities cannot be expressed precisely in the analytical models when load is applied from the outside to the inside.

Figure 59 shows the computed results of the deflected shapes of the member along the span when load is applied from the inside. The deflection under elastic state of the members are naturally in accordance with the elastic structural analysis. After cracks occurred, however, the deflection gradually differs from that obtained by the elastic analysis. Namely, the deflection is concentrated at the midspan where cracks are initiated. The result shows good agreement with the experimental deflection mentioned in **4.3.**

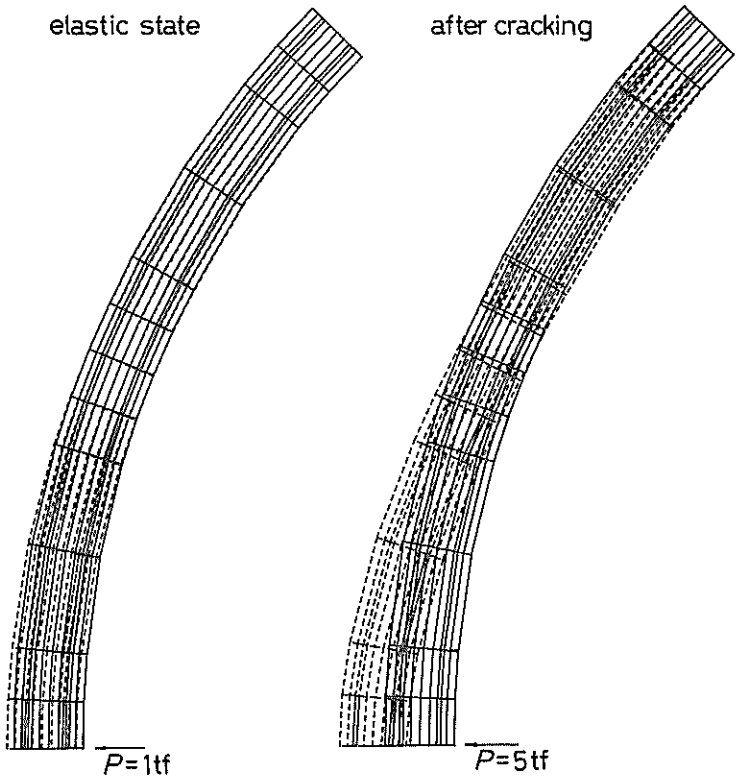

Fig. 59 The Computed Deflection

7.3 Strain

Load-tensile strain curves in reinforcing bars at the midspan are shown in Fig. 60. The computed strain is defined as the calculated axial strain in the reinforcing bar elements. When load is applied from the inside, the computed and experimental results show good agreement. Hence the appropriateness of the assumptions for modeling reinforcing bars and the bond stress transmission between concrete and reinforcing bars is confirmed. When load is applied from the outside, the computed strain is considerably small in comparison with the experimental strain at the same load, in case that the isotropic elements are used for the reinforcing bars. Another computed strain by FEM-2 is in accordance with the experimental strain. The modeling for reinforcing bar to be transmitting the axial force only may explain the characteristic of the strain in reinforcing bar well, and these assumptions for reinforcing bars in the arc-shaped member are confirmed.

Figure 61 shows the distributions along the span of the computed and experimental strain in reinforcing bars. The computed and experimental results show good agreement for both cases when load is applied from the outside and when load is applied from the inside. However, when load is applied from the outside, the computed strain by the ordinary isotropic model in the vicinity of the midspan is considerably smaller than the experimental strain. The difference between the computed and experimental results is considered to be resulted from the large radial stress calculated by

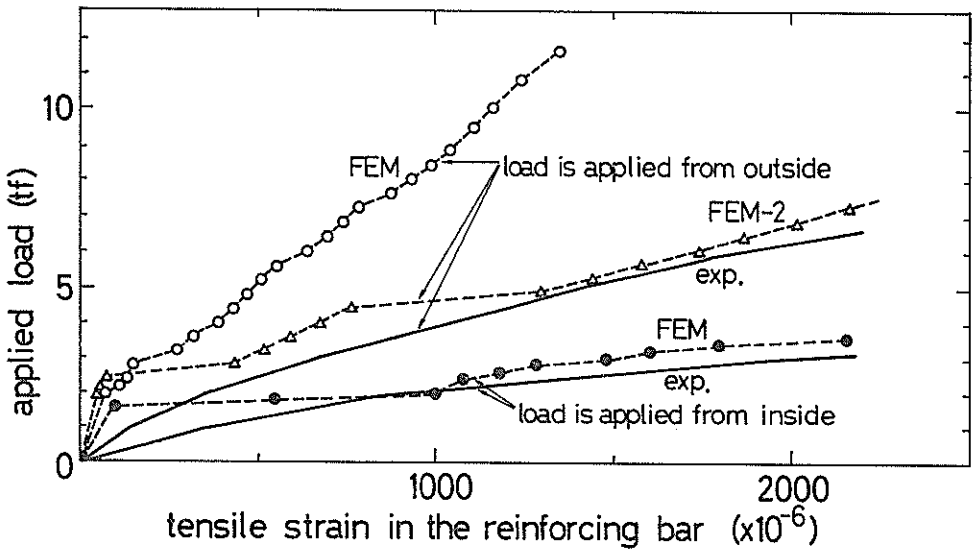

Fig. 60 The Computed and Experimental Load-Strain Curves in the Reinforcing Bars

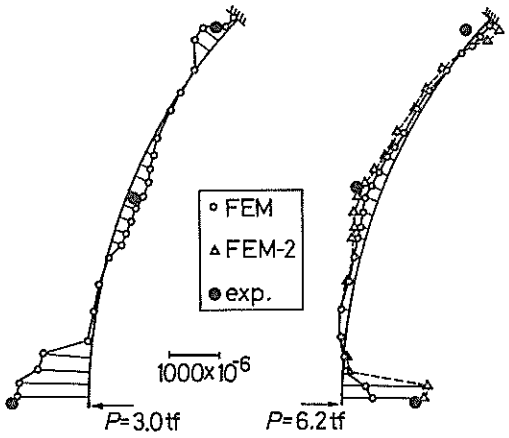

Fig. 61 Distribution of Strain in Reinforcing Bar along the Span

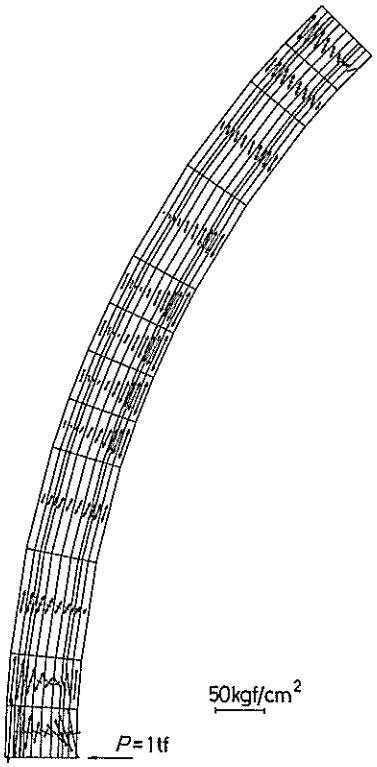

Fig. 62 The Computed Principal Stress in the Elastic State when Load is Applied from Inside

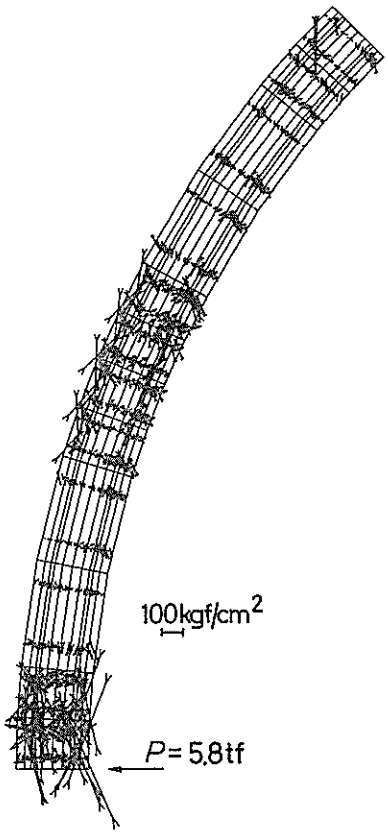

Fig. 63 The Computed Principal Stress when Load is Applied from Inside

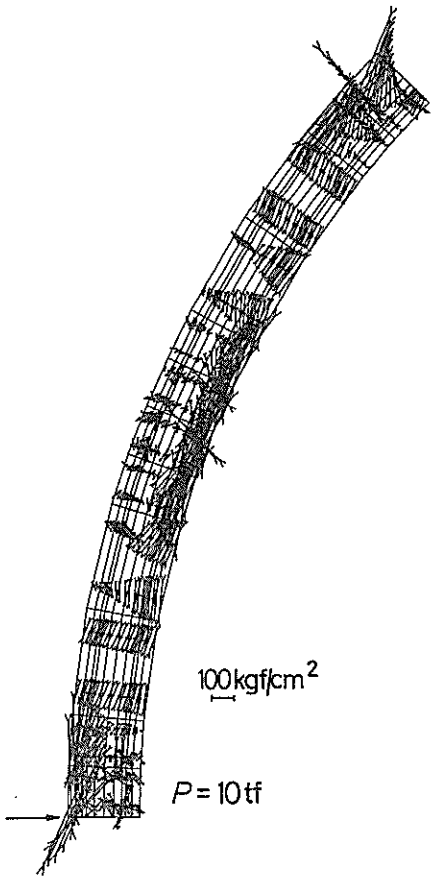

Fig. 64 The Computed Principal Stress when Load is Applied from Outside

the analysis at the midspan.

The computed results of principal stresses are shown in Figs. 62, 63 and 64. Under elastic state shown in Fig. 62, circumferential strains (stresses) are calculated both in concrete and in reinforcing bars. For radial strains, on the other hand, their values are considerably smaller than those of circumferential strains. Moreover, under plastic state, nearly at the ultimate, large radial compressive stress is calculated at the midspan and the quarter span. When load is applied from the outside, the end of the member also has large radial compressive stresses. The elements for reinforcing bar resist the radial stress in the ordinary plane stress model, and result in that the apparent stiffness of reinforcing bar will be evaluated very large. Therefore, the application of the anisotropic constitutive model to the elements for reinforcing bar gives more precise results as described previously.

7.4 Crack

Figure 65 shows the computed and experimental crack formations. The propaga-

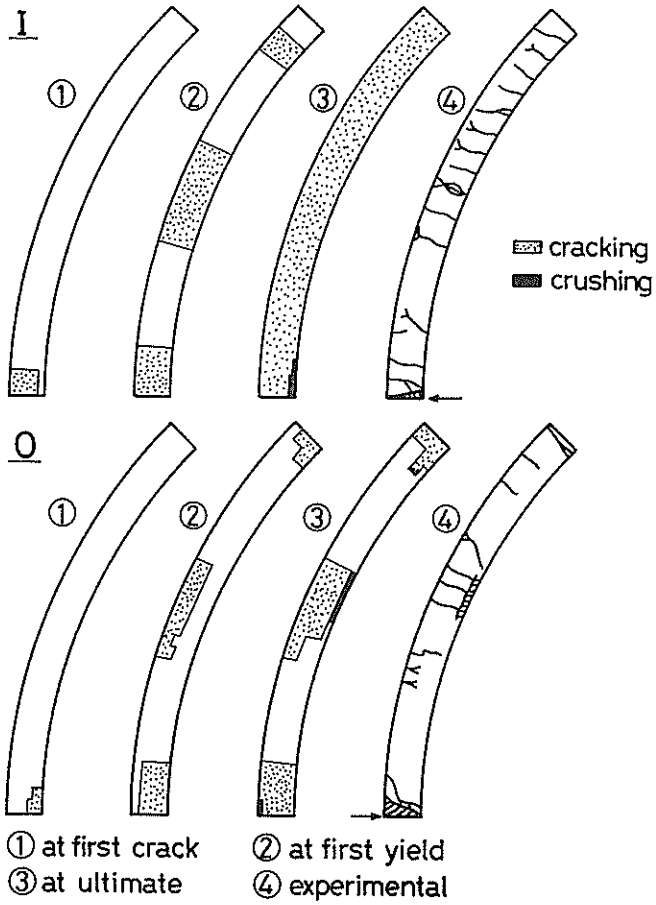

Fig. 65 The Computed and Experimental Crack Formation when Load is Applied from Inside (I) and from Outside (O)

tion and widths of cracks cannot be estimated precisely, because the smeared cracking model is adopted. The zone of crack formation and development, therefore, can be investigated in the smeared cracking model. When load is applied from the inside, the computed cracks are initiated near the midspan at first, and then cracks are formed at the quarter span and the end of the member. After that, cracks are formed and propagate gradually in the concrete elements in turn as the load is increased. Being near at the ultimate, all the concrete elements have cracks, and then the crushing of concrete occurs on the inner surface of the member at the midspan at the ultimate. These results are in accordance with the experimental results.

When load is applied from the outside, cracks are initiated on the inner surface of the member near the midspan and propagate towards the outside fiber as the load is increased. At the first yield of reinforcing bar, not only the midspan but also the quarter span and the end of the member have cracks. Just before at the ultimate, cracks develop and propagate rapidly at the above mentioned three sections. Being different

from the results when load is applied from the inside, cracks concentrate in these parts, and the others have no cracks. Crushing of concrete occurs on the outer surface of concrete at the midspan and on the inner surface of concrete at the quarter span. These results are in accordance with those of the experiment.

Evident shear cracks are formed at the midspan in the experiment. Cracks by the analytical model cannot be separated into shear cracks and flexural cracks. However, large shearing stresses are calculated at the midspan. Consequently, the shear failure of concrete is predicted at the midspan by the computed results.

7.5 Discussion

The macrocracking patterns and crushing of concrete are well predicted for the arc-shaped members under each direction of loading as discussed in **7.4.** In the elastic analysis method, which is usually used in design works, the largest, the second largest and the third largest values of the bending moment are calculated at the midspan, at the endspan and at the quarter span, respectively. The nonlinear analytical results, however, show that the fracture of the member occurs at the midspan, and then at the quarter span. The redistribution of the bending moment occurs in the region between the quarter spans. These analytical results are in accordance with the experimental results. The fracture process which is observed in the loading test, therefore, cannot be examined by the elastic analysis.

The fracture process of the member is related to the plastic hinge formation. Plastic hinges are formed after reinforcing bars yielded and concrete is crushed. The arc-shaped member turns into two cantilever beams after a plastic hinge occurs at the midspan. Namely, after the formation of plastic hinges, the sections have abilities of large deformation and rotation. Furthermore the bending moment at the midspan will be distributed towards the ends of the member. The mechanism of failure must be incorporated in the analytical model in the case where plastic hinges are formed. The analytical results with the adoption of the above mechanism are in accordance with the experimental results and the propriety of modeling for the arc-shaped member can be confirmed.

8. Conclusions

This report describes the loading test and numerical analysis by the finite element method for arc-shaped members. The following conclusions are obtained from the experimental and analytical work.

1) The fracture process of the arc-shaped member differs from that of the straight member because of the influence of curvatures of the member. Moreover the fracture process depends on the directions of the loadings.
2) When load is applied from the outside to the inside, the failure mode of the member is crushing and shear failure of concrete at the midspan section, and crushing of concrete at the quarter span sections. When load is applied reversely, cracks pass through some sections near the midspan and the member is considered to be divided into two cantilever beams. The flexural failure dominates in the member at this loading condition.
3) The first yield and ultimate load of the member when load is applied from the outside to the inside are larger than those when load is applied reversely. The ductility factor is defined as the ratio of the deflection at the first yield load to the deflection at the ultimate load. The ductility factor is 2 to 3 when load is applied from the

outside to the inside. However, the ductility factor is 12 to 14 when load is applied from the inside to the outside. When load is applied alternately, the ductility factor is near that of the loading from the outside to the inside.

4) The energy absorption ability is indicated by the equivalent viscous damping coefficients. These coefficients can be obtained from the hysteresis loops of the load-deflection relationship. The difference of directions of loading does not affect the equivalent viscous damping coefficients; the values of the coefficients are 4 to 6%.
5) The applied load, from the outside to the inside, at a maximum crack width of 0.2 mm is greater than that from the inside to the outside. The maximum crack width is generally in proportion to the strain in tensile reinforcing bar. However, when load is applied from the outside to the inside, the increment of the maximum width of crack increases like parabola.
6) The ultimate strengths of the members calculated by the limit state design for characteristic values of materials and loads are 0.8 to 0.9 times as large as those by the loading tests. At this time, the fracture resisting bending moment is defined as the value when plastic hinges are formed at the quarter span. Moreover, the bending moment when a plastic hinge is formed at the midspan and the distributed bending moment after plastic hinge formation must be considered. The flexure and shear strength of the section of the member can be calculated by the ordinary limit state design method which is applied to straight members.
7) The crack width is very important for the durability of the members. The maximum crack width of 0.2 mm is one of the limitations of offshore structures according to the "Limit State Design of Concrete Structures." The maximum cracks in the loading tests are smaller than those calculated by the formula suggested in this design code up to 0.2 mm of crack width. Namely, the formula gives the maximum width of crack on the safe side.
8) The finite element method in this report takes into account the nonlinearity of the materials and the formation of plastic hinges. The results by this analytical method can explain fairly well the fracture process of the arc-shaped member. The load-deflection relationship of the member, load-strain relationship in the reinforcing bar, behavior of crack formation and so on can be estimated by this analytical method.
9) The applicability of the finite element method to the arc-shaped member is confirmed. However, in order to predict the behavior of the member more precisely, the bond-slip property between concrete and bars, transmission mechanism of shear force at the crack face, rigidity at unloading stage, etc. must be taken into account in the calculation model.

Acknowledgements

The research reported herein was made possible by the financial support of the special research project, "Study on Analysis of Gravity Type Structures in Deep Waters."

Assistance of Mr. Hideo NISHIZAWA (member of Subaqueous Tunnels and Pipelines Laboratory, Structures Division) in the experimental work is fully acknowledged.

(Received on Nov. 30, 1984)

References

1) YOKOTA, H. and O. KIYOMIYA: Vibration and Stress in Curved Slit Caisson Type Breakwater, *Proc. of the 37th Annual Conference of the JSCE*, Oct. 1982, pp. 431～432 (*in Japanese*).
2) DAWOUD, R. H.: Flexural Stresses in Rectangular Reinforced Concrete Curved Members, *ACI Journal*, Mar. 1970, pp. 237～242.
3) KAWAKAMI, M., M. KAGAYA and H. TOKUDA: Plastic Design of Reinforced Concrete Curved Members, *Concrete Journal*, Vol. 18, No. 5, May 1980, pp. 111～120 (*in Japanese*).
4) HEGER, F. J. and T. J. MCGRATH: Radial Tension Strength of Pipe and Other Curved Flexural Members, *ACI Journal*, Jan.–Feb. 1983, pp. 33～39.
5) LOVE, A. E. H.: *A Treatise on the Mathematical Theory of Elasticity*, Cambridge Univ. Press, 1892.
6) TIMOSHENKO, S. and S. W. KRIEGER: *Theory of Plates and Shells*, 2nd ed., McGraw-Hill Kogakusha, 1959, 580 p.
7) LUNDGREN, H.: *Cylindrical Shells*, Corona Book Company, 1962.
8) Construction Division, Ports and Harbours Bureau, Ministry of Transport: *Technical Research Report of Prestressed Concrete Port and Harbour Structures*, Mar. 1980, pp. 51～87.
9) Japan Society of Civil Engineers: Recommendations for Limit State Design of Concrete Structures (provisional), *Concrete Library* No. 52, Nov. 1983, 369p. (*in Japanese*).
10) Ports and Harbours Bureau and Port and Harbour Research Institute, Ministry of Transport: *Technical Standards for Port and Harbour Facilities in Japan*, Apr. 1980, p. 3–22.
11) TANIMOTO, K. et al.: A Hydraulic Experimental Study on Curved Slit Caisson Breakwaters, *Report of the Port and Harbour Research Institute*, Vol. 19, No. 4, Dec. 1980, pp. 3～53 (*in Japanese*).
12) Construction Division, Ports and Harbours Bureau, Ministry of Transport: Design Criteria for Prestressed Concrete Port and Harbour Structures (provisional), *Technical Research Report of Prestressed Concrete Port and Harbour Structures*, Mar. 1980, pp. 12～50 (*in Japanese*).
13) Japan Society of Civil Engineers: Recommendations for Limit State Design of Concrete Structures (provisional), *Concrete Library* No. 52, Nov. 1983, pp. 73～78 (*in Japanese*).
14) Japan Society of Civil Engineers: *Standard for Prestressed Concrete Structures*, Jan. 1979, 210p. (*in Japanese*).
15) CEB and FIP: *CEB-FIP MODEL CODE FOR CONCRETE STRUCTURES*, CEB-FIP International Recommendations 3rd Edition (1978), pp. 156～160.
16) YAMADA, Y.: *Plasticity and Viscoelasticity*, Baifukan, 1972, 240p. (*in Japanese*).
17) YOKOTA, H. and O. KIYOMIYA: Non-linear Analyses of Reinforced Concrete Members by Finite Element Method, *Technical Note of the Port and Harbour Research Institute*, No. 460, Sept. 1983, 34p. (*in Japanese*).
18) ASCE: State-of-the-Art Report on *FINITE ELEMENT ANALYSIS OF REINFORCED CONCRETE*, 1982, 545p.
19) CHEN, W. F.: *Plasticity in Reinforced Concrete*, McGraw-Hill Book Company, 1982, 474p.
20) KUPHER, H., H. K. HILSDORF and H. RUSCH: Behavior of Concrete Under Biaxial Stresses, *ACI Journal*, Vol. 66, No. 8, Aug. 1969, pp. 656～666.
21) WASHIZU, K. et al.: *Finite Element Method Handbook II*, Baifukan, 1981, pp. 171～302 (*in Japanese*).

22) KIYOMIYA, O., H. YOKOTA and H. NISHIZAWA: Ultimate Strength and Toughness of Arc Shaped Wave Dissipating Members, *Transactions of the Japan Concrete Institute*, Vol. 5, 1983, pp. 457～464.
23) OKADA, K, M. FUJII and K. KOBAYASHI: *Prestressed Concrete Structure*, Kokuminkagakusha, 1979, pp. 65～82 (*in Japanese*).
24) NAAMAN, A. E.: *Prestressed Concrete Analysis and Design*, McGraw-Hill Book Company, 1982, pp. 275～316.

List of Symbols

$A_{c,ef}$: effective embedded zone where reinforcing bars can effectively influence the crack widths
A_s : area of reinforcement contained in $A_{c,ef}$
A_{sc} : area of compression reinforcement
A_{st} : area of tension reinforcement
A_w : area of web reinforcement
$[B]$: element strain-nodal displacement matrix
b_w : width of member
C' : resultant compressive force in the concrete section due to applied external forces
c : concrete cover for embedded bars
c_ϕ : spacing of bars
$[D^e]$: elastic material stiffness matrix
$[D^{ep}]$: elastic-plastic material stiffness matrix
d : effective depth of member
d_c : distance from extreme compressive fiber to centroid of compressive reinforcement
E_c : secant modulus of elasticity of concrete
E_{ci} : initial modulus of elasticity of concrete
E_p : modulus of elasticity of prestressing steel
E_s : modulus of elasticity of reinforcement
$\{\Delta F\}$: incremental nodal force vector
f : failure criterion or yield function
f_b : flexural strength of concrete
f_c' : compressive strength of concrete at loading test
f_{cd}' : design compressive strength of concrete
f_{ck}' : characteristic compressive strength of concrete
f_{ct} : tensile strength of concrete
f_{cy}' : compressive yield strength of concrete
f_{pud} : design tensile strength of prestressing steel
f_{vd} : design shear strength of concrete
f_{vod} : apparent design shear strength of concrete
f_{wyd} : design yield strength of web reinforcement
f_y : specified yield strength of reinforcement
f_{yd} : design yield strength of reinforcement
G : shear modulus
g : plastic potential
H : wave height
H' : hardening parameter

H_{max} : maximum wave height
$H_{1/3}$: significant wave height
h : overall thickness or depth of member
h : positive constant
h_e : equivalent viscous damping coefficient
J_1 : first invariant of the stress deviator tensor
J_2 : second invariant of the stress deviator tensor
K : constant ($=600\times10^3$ kgf/cm^2)
K : average stiffness of member
$[K]$: structural stiffness matrix
$[K^{ep}]$: elastic-plastic structural stiffness matrix
K_r : spring constant of bond-link element related to dowel action
K_s : spring constant of bond-link element related to interface shear stiffness
K_0 : initial stiffness of member
K_1 : coefficient expressing influence of bond behavior of reinforcement (0.4 for deformed bars, 0.8 for round bars)
K_2 : coefficient for the influence of the form of the stress diagrams (0.125 in bending, 0.25 for pure tension, $0.25(\varepsilon_1+\varepsilon_2)/2\varepsilon_1$ in eccentric tension or for a zone of the web of a beam)
k_1 : coefficient ($=0.85$)
k_3 : coefficient expressing influence of bond behavior of reinforcement (1.0 for deformed bars, 1.3 for round bars and PC bars)
M : bending moment in general at section considered
M_c : bending moment at the midspan section due to external force
M_d : design bending moment of resistance
M_u : strength design moment
M_0 : bending moment at decompression
N : loading incremental step in finite element method
N : axial force in general at section considered
N_c : axial force at the midspan section due to external force
N_u' : axial compressive force of resistance
P : concentrated external load in general
$P_{A,B}$: wave pressure at points A and B
P_c : applied load at cracking
P_u : applied load at ultimate
P_w : resultant wave force
P_y : applied load at first yield
p_w : reinforcement ratio ($=A_s/b_w\cdot d$)
$[R]$: unbalanced nodal force vector
S_{rm} : average distance between cracks
s : spacing of web reinforcement
T_{sc}' : resultant compressive force in compressive reinforcement due to external force
T_{st} : resultant tensile force in tension reinforcement due to external force
$T_{1/3}$: significant wave period
$\{\Delta U\}$: incremental nodal displacement vector
V_d : design shear force of resistance
V_{cd} : design shear force of resistance in concrete
V_{yd} : design shear force of resistance in web reinforcement

W_{oa} : cumulative dissipated energy in the member
W_d : dissipated energy in the member
W_i : loading energy
w : crack width in general
w_k : characteristic crack width
w_m : mean crack width
w_0 : unit weight of sea water
x : neutral axis depth
z : distance from the centroid of resultant compressive force in concrete to the centroid of tension reinforcement
α : coefficient concerned the first invariant of the stress deviator in the Drucker-Prager criterion (=0.07)
α : angle between inclined stirrups and longitudinal axis of member
β : coefficient related to the centroid of resultant compressive force in concrete (=0.4)
β : reduction factor related to modulus of elasticity of concrete
β_a : coefficient related to effective depth being investigated for shear strength
β_n : coefficient related to axial force being investigated for shear strength
β_p : coefficient related to reinforcement ratio being investigated for shear strength
β_1 : coefficient related to bond properties of bars (=1/2.5 K_1)
β_2 : coefficient related to the influence of the duration of the application or repetition of the loads
(1 at first loading, 0.5 for load applied in a sustained manner or for a large number of load cycles)
γ_a : coefficient (=1.2)
γ_b : coefficient (=1.15 in general)
γ_c : material factor for concrete
γ_m : material factor for steel
δ : midspan deflection in general
δ_u : midspan deflection at ultimate
δ_y : midspan deflection at first yield
$\{\Delta\varepsilon\}$: strain incremental vector
ε_0' : compressive strain in concrete
ε_{cc}' : compressive strain in extreme compression fiber of concrete
ε_p : strain in prestressing steel
$\{d\varepsilon_p\}$: incremental plastic strain vector
ε_s : strain in reinforcing bar
ε_{sc}' : compressive strain in reinforcing bar
ε_{sm} : mean elongation
ε_{st} : tensile strain in reinforcing bar
ε_{sy} : yield strain of reinforcing bar
$\varepsilon_{1,2}$: concrete strains calculated for cracked section
θ : angle in general
ν : Poisson's ratio
π : circular constant (=3.1416)
ρ_r : reinforcement ratio
$\{\Delta\sigma\}$: stress incremental vector
σ_c' : compressive stress of concrete
σ_{ij} : stress tensor

σ_p : stress in prestressing steel
σ_s : stress in reinforcement in general
$\Delta\sigma_s$: stress increment in reinforcement in the cracked section being investigated for crack width
σ_{sc} : stress in compressive reinforcement
$\Delta\sigma_{s0}$: stress in reinforcement calculated on the assumption of a cracked section where the maximum tensile stress in the concrete (uncracked section) is taken equal to f_{ct}
σ_{st} : stress in tensile reinforcement
σ_x : axial stress in the x direction
σ_y : axial stress in the y direction
σ_z : axial stress in the z direction
$\{\sigma_0\}$: released stress vector during fracture (cracking or crushing)
$\sigma_{1,2}$: principal stress
$\tau_{xy,\,yz,\,zx}$: shear stress
ϕ : diameter of steel or diameter in general

Appendix A Calculation of the Prestressing Force

Prestressing force in the arc-shaped member must be estimated considering various kinds of prestress loss. The following three factors are taken into consideration for the introduction of prestressing force in the test specimen.

① elastic deformation of concrete

$$\Delta\sigma_{pi}=\frac{1}{2}n_p\sigma_{ci}\frac{N-1}{N} \tag{A.1}$$

$$\sigma_{ci}=\frac{A_p\sigma_{ci}}{A_c}+\frac{A_p\sigma_p e_p^2}{I_c} \tag{A.2}$$

② frinction between prestressing bar and sheath (Fig. A.1)

$$P_x=P_i e^{-(\mu\alpha+\lambda x)} \tag{A.3}$$

③ slip at the ancharage system

$$\Delta P=\frac{\Delta l}{l}A_pE_p \tag{A.4}$$

Further, the effective prestress which is resulted from the time dependent loss is estimated by other three factors ④ to ⑥.

④ creep of concrete

⑤ drying shrinkage of concrete

⑥ relaxation of prestressing bar

$$\Delta\sigma_p=\frac{n_p\varphi_t(\sigma_{cd}+\sigma_{cpt})+E_p\varepsilon_{cs}}{1+n_p(\sigma_{cpt}/\sigma_{pt})(1+(\varphi_t/2))}+\gamma\sigma_{pt} \tag{A.5}$$

In the fabrication of the PC specimens, the constants in above equations are

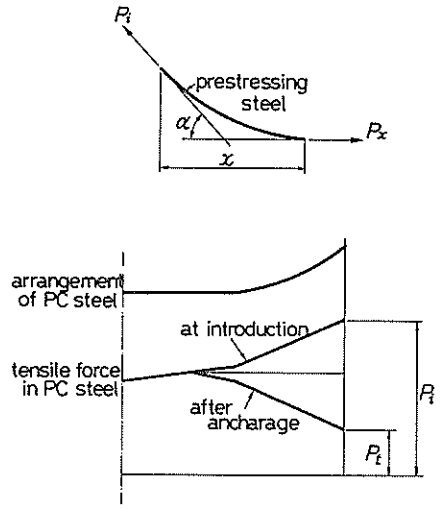

Fig. A.1 Friction between Prestressing Steel and Sheath, and Tensile Force in Prestressing Steel at Ancharage

decided as follows. The initial prestressing force immediately after introduction of prestress is the factors ④ to ⑥ and the objective effective prestress of 20 kgf/cm² at the time of loading test.

$$n_p=E_p/E_c=2.0\times10^6\ \text{kgf/cm}^2/3.0\times10^5\ \text{kgf/cm}^2=6.67$$

$$\varepsilon_{cs}=200\times10^{-6}$$

$$\varphi_t=1.9$$

$$\gamma=0.03$$

$$\sigma_{cd}\fallingdotseq0$$

$$\sigma_{cpt}=\frac{P_t}{A_c}+\frac{P_te_p}{I_c}=\frac{P_t}{297}\quad(e_p=0)$$

$$\sigma_{pt}=\frac{P_t}{A_p}=\frac{P_t}{1.9}$$

$$\therefore\quad \Delta\sigma_p=\underbrace{0.039P_t+369.3}_{\text{creep and shrinkage}}+\underbrace{0.0158P_t}_{\text{relaxation}}\quad(\text{kgf/cm}^2)$$

$$\sigma_{pe}=\frac{297\times20}{1.9}=3126\ \text{kgf/cm}^2$$

$$\sigma_{pe}=\sigma_{pt}-\Delta\sigma_p$$

$$\therefore\quad P_t=7418\ \text{kgf}$$

Consequently, the initial prestressing force is 7418 kgf (total).

The mechanical loss ① to ③ are estimated as follows:

$$\Delta\sigma_{ci}=\frac{A_p\sigma_{pi}}{A_c}=\frac{P_t'}{297}$$

$$N=2$$

$$\Delta\sigma_{pi}=\frac{1}{2}\times6.67\times\frac{P_t'}{297}\times\frac{1}{2}=5.614\times10^{-3}P_t'$$

$$P_x=P_t'e^{-(0.3\times0.785+0.003\times1.456)}=0.787P_t'$$

$$\Delta P=\frac{\Delta l}{l}A_pE_p=0\quad(\Delta l=0\ \text{because of the nut ancharage})$$

$$\therefore\quad 0.787P_t'-5.614\times10^{-3}P_t'\times1.9=P_t$$

$$P_t'=9555\ \text{kgf}$$

Thus, the objective strain in the PC bar immediately after the introduction of prestressing is calculated to be $P_t/2/E_p=1855\times10^{-6}$.

Control for prestressing force is conducted by the above strain in the prestressing bar at the midspan.

Notations

A_c : area of concrete
A_p : area of prestressing steel
E_c : modulus of elasticity of concrete
E_p : modulus of elasticity of prestressing steel
e_p : eccentricity of the prestressing force
I_c : moment of inertia of uncracked concrete section

l : total length of prestressing steel
Δl : slip of prestressing steel
N : numbers of prestress introduction
n_p : modular ratio E_p/E_c
$P_{i,x}$: prestressing force at the end of prestressing steel (i) or at section x
P_t : final prestressing force at introduction
P_t' : initial prestressing force at introduction
α : total angular change of prestressing steel between two points (radian)
γ : relaxation coefficient
ε_{cs} : concrete strain due to drying shrinkage
λ : coefficient in prestress loss
μ : curvature friction coefficient
σ_{ci} : compressive stress at the centroid of prestressing steel due to prestress
σ_{cd} : compressive stress at the centroid of prestressing steel due to permanent load
σ_{cpt} : compressive stress at the centroid of prestressing steel due to prestressing
$\Delta\sigma_{pi}$: reduction of average tensile force in prestressing steel
σ_{pt} : stress in prestressing steel due to the final prestressing force
φ_t : creep coefficient

Appendix B Distribution of Prestress in the Specimen

It is difficult to estimate the distribution of prestress in the arc-shaped member. Measurement of strains along prestresing bars in the arc-shaped member is carried out at the introduction of prestressing to know the distribution of prestress. The location of measurement is shown in Fig. B.1.

Measured strains at the introduction in prestressing and reinforcing bars are shown in Figs. B.1 to B.5. First, prestressing force is introduced in the prestressing bar A, and then in the prestressing bar B.

Moreover the variation of prestress with the lapse of time is shown in Fig. B.6.

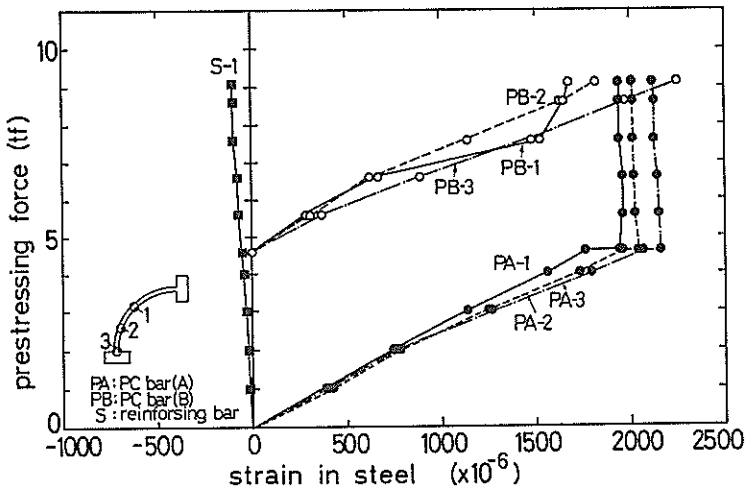

Fig. B.1 Strain in Steel at the Prestressing (PC-1)

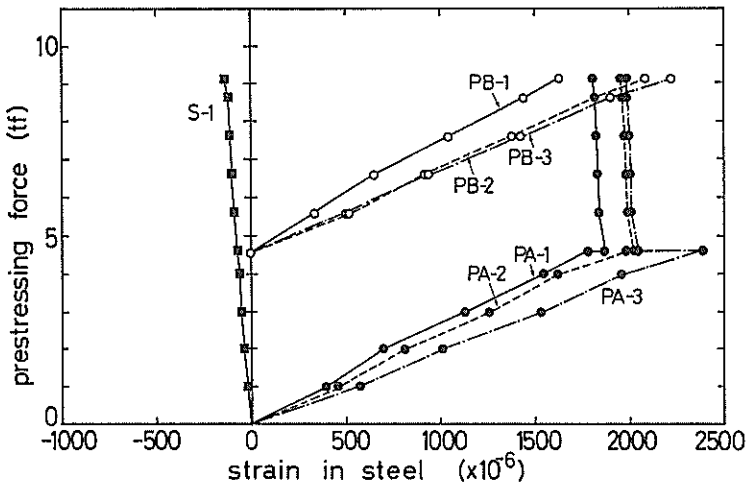

Fig. B.2 Strain in Steel at the Prestressing (PC-2)

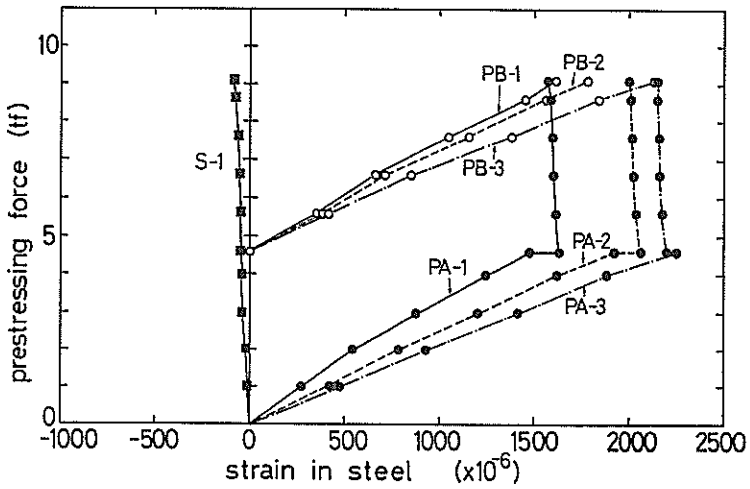

Fig. B.3 Strain in Steel at the Prestressing (PC-3)

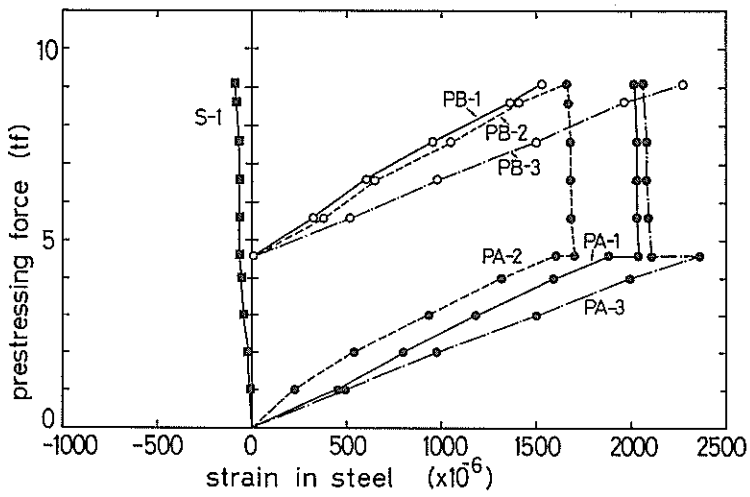

Fig. B.4 Strain in Steel at the Prestressing (PC-4)

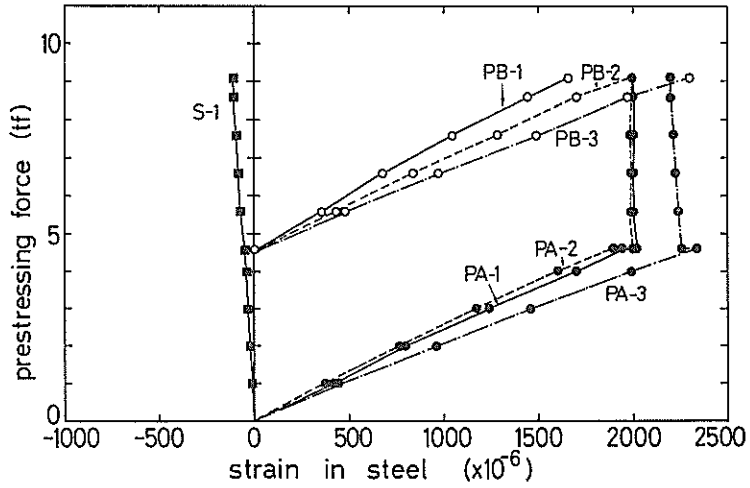

Fig. B.5 Strain in Steel at the Prestressing (PC-5)

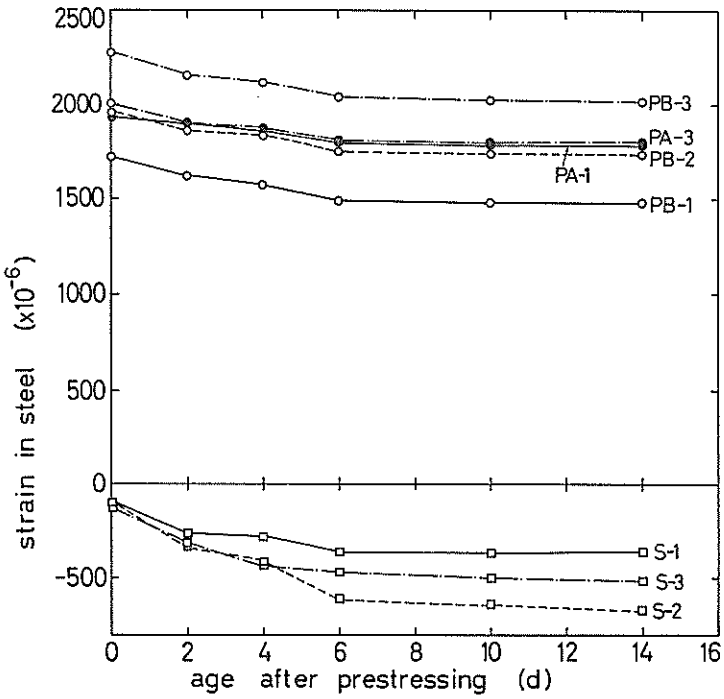

Fig. B.6 Variation of Strain in Steel After the Prestressing